Carbon Capture Science & Technology 13 (2024) 100329

Contents lists available at ScienceDirect

Carbon Capture Science & Technology

journal homepage: www.elsevier.com/locate/ccst

Full Length Article

Pore-scale study of CO_2 desublimation in a contact liquid

Timan Lei[a], Geng Wang[b], Junyu Yang[a], Jin Chen[a], Kai H. Luo[a,*]

[a] Department of Mechanical Engineering, University College London, Torrington Place, London WC1E 7JE, UK
[b] National Microgravity Laboratory, Institute of Mechanics, Chinese Academy of Sciences, Beijing 100190, China

ARTICLE INFO

Keywords:
Cryogenic carbon capture
Multiphysics lattice Boltzmann method
CO_2 desublimation
Two-phase flow
Pore scale modelling

ABSTRACT

Cryogenic carbon capture (CCC) designed to operate in a contact liquid is an innovative technology for capturing CO_2 from industrial flue gases, helping mitigate climate change. Understanding CO_2 desublimation properties in a contact liquid is crucial to optimizing CCC, but is challenging due to the complex physics involved. In this work, a multiphysics lattice Boltzmann (LB) model is developed to investigate CO_2 desublimation in a contact liquid for various operating conditions, with the multiple and fully-coupled physics being incorporated (i.e., two-phase flow, heat transfer across three phases, CO_2 transport between the gas and liquid, homogeneous and heterogeneous desublimation of CO_2, and solid CO_2 generation). The CO_2 desublimation process in a contact liquid is well reproduced. Moreover, parametric studies and quantitative analyses are set out to identify optimal conditions for CCC. The decreasing liquid temperature (T_l) and flue gas temperature (T_0) are found to accelerate the CO_2 desublimation rate and enhance the CO_2 capture velocity (v_c). However, excessively low T_l and T_0 values should be avoided. These conditions increase the energy consumption of cooling while only marginally improving v_c, due to the limited CO_2 supply. The CCC system performs effectively when purifying flue gases with high CO_2 content (Y_0). This is because the large Y_0 accelerates the CO_2 desublimation rate and enhances the overall CO_2 capture efficiency. A high gas injection velocity (or Pe) is beneficial for amplifying v_c by increasing the gas–liquid interfaces and enhancing the CO_2 supply. Nevertheless, too high a Pe should be avoided, as it hinders the transport of CO_2 to the liquid or solid CO_2 surfaces, ultimately restricting the amount of CO_2 available for desublimation and inhibiting the enhancement of v_c. This study develops a viable LB methodology to investigate CO_2 desublimation in a contact liquid for varying conditions, which advances the knowledge base of CCC and facilitates its industrial applications.

1. Introduction

Climate change is widely recognized as one of the most pressing environmental challenges. There is a consensus among researchers that such an issue is mainly caused by human activities that yield critical CO_2 emissions (Kamkeng et al., 2021; Lei et al., 2023; Mac Dowell et al., 2017). To mitigate anthropogenic CO_2 emissions, various carbon capture technologies have been developed, including absorption, membrane, adsorption, and cryogenic processes (Bose et al., 2024; Naquash et al., 2022). Cryogenic carbon capture (CCC), as a relatively emerging technology, has garnered increasing research interest. Among the existing CCC designs, the one utilizing direct contact heat exchangers (or cryogenic liquids) is operationally simple (Fazlollahi et al., 2017; Jensen, 2015). During the operation of liquid-based CCC, the flue gas containing multiple components is injected into the CCC system and cooled by the liquid to low temperatures. This subsequently induces the desublimation of CO_2 and produces solid CO_2 particles within the liquid. Finally, these solid CO_2 particles are separated from the liquid and recycled for further applications. This system presents significant application potentials and research interests due to its numerous advantages, like low energy penalty, process simplicity, cost-effectiveness, and absence of chemicals (Font-Palma et al., 2021; Jensen et al., 2015). Nevertheless, the development of CCC is still in its nascent stage because of technical problems and knowledge gaps, including inappropriate operating conditions, hydrocarbon emissions, and unclear desublimation kinetics (Jensen, 2015; Pan et al., 2013). Therefore, investigating CO_2 desublimation in the liquid-based CCC system is crucial to advancing the understanding of CCC and providing guidance for its development.

The problem of CO_2 desublimation in a contact liquid involves several fully-coupled physics, i.e., two-phase flow, heat transfer across three phases (i.e., contact liquid, flue gas, and solid CO_2), multicomponent transport between the flue gas and contact liquid, homogeneous desublimation within the contact liquid, heterogeneous desublimation on solid CO_2 surfaces, and solid CO_2 generation. For such a complex problem, some experimental and numerical efforts have been devoted to gaining a comprehensive understanding.

* Corresponding author.
E-mail address: k.luo@ucl.ac.uk (K.H. Luo).

https://doi.org/10.1016/j.ccst.2024.100329
Received 25 August 2024; Received in revised form 20 October 2024; Accepted 21 October 2024

Tuinier et al. (2011a, 2010, 2011b) designed a CCC system using three dynamically operated packed beds for purifying flue gases at the atmospheric pressure. Their experiments demonstrated that the operational cost strongly depended on the initial bed temperature and the CO_2 concentration in the flue gas. Meanwhile, they proposed a one-dimensional (1D) model to solve the mass and energy balance during the desublimation of CO_2 on packed bed surfaces. They indicated that an initial bed temperature above −120°C could exponentially diminish the amount of solid CO_2 captured and strongly amplify the specific cooling duty (Tuinier et al., 2011b). However, such CCC systems were constrained to the atmospheric pressure and gases with low CO_2 contents. For this concern, Ali et al. (2016, 2014) designed a multiple cryogenic desublimation based pipeline network to remove H_2O and CO_2 from flue gases with high CO_2 contents and high pressures. In parallel, another CCC system based on Stirling coolers (SC) was developed for CO_2 capture (Song et al., 2012a; 2014; 2013; 2012b). After conducting extensive experiments, the optimal gas flow rate and SC temperatures were identified for the gas cooling stage to optimize the system performance. A two-dimensional (2D) model was built to examine the growth of CO_2 frost layers on SC surfaces, demonstrating that the accumulated frost layer on SC increased the thermal resistance and raised the surface temperature (Song et al., 2013).

The above findings advanced the knowledge base of CO_2 desublimation on solid surfaces, but failed to explore CO_2 desublimation properties within a contact liquid. To cover this void, the feasibility and efficiency of the liquid-based CCC system was explored. Jensen *et al.* Jensen (2015), Jensen et al. (2015) proposed a CCC system with an external cooling loop to cool the contact liquid for subsequent CO_2 desublimation. They employed computational simulations and experimental validations to demonstrate that this system was capable of removing up to 99% of CO_2 from the flue gas continuously while maintaining low energy penalties. A CCC natural-gas treatment system was then designed for capturing CO_2 from the natural gas (Fazlollahi et al., 2017). Through experimental and numerical investigations, it was recommended that the high operating pressure and the low methane content in natural gas were beneficial for improving the CO_2 capture performance. More recently, a 1D model incorporating a new mass deposition scheme was proposed to consider both the heterogeneous nucleation of solid CO_2 on the gas–solid interface and the homogeneous nucleation within the gas phase (Debnath et al., 2019). The condensed CO_2 thickness was simulated and mapped over the space-time domain, based on which spatiotemporal evolutions of the gas phase fraction and the CO_2 separation strength were further calculated.

These existing studies have evaluated the CO_2 capture performance in a contact liquid to a certain extend. Despite these achievements, the multiple physics behind CO_2 desublimation and their complex interactions have not been thoroughly examined across extensive operating conditions. Moreover, the current simulations were conducted on volume-averaged scales, ignoring pore-scale details, such as the flow of gas bubbles within liquid, intricate structures of solid CO_2, conjugate heat transfer across three phases, and CO_2 transport from the gas to liquid phases. The pore-scale information, however, is crucial to accurately constructing empirical correlations required in volume-averaged simulations (Xu et al., 2018a; 2018b; Yang et al., 2021). Therefore, it is essential to develop pore-scale models for comprehensively investigating the underlying physics of CO_2 desublimation in a contact liquid.

Over the past three decades, the lattice Boltzmann (LB) method has been developed into a powerful alternative to conventional solvers for simulating complex fluid flows with phase change in porous media at the pore scale (Chen et al., 2022; Lei et al., 2019; Li et al., 2016; Wei et al., 2022). This is attributed to its distinctive advantages. For instance, the LB method, based on the kinetic theory, can seamlessly handle multiple physics, including multiphase flow, phase change, and heat and mass transfer. Additionally, elementary mechanical rules (e.g., bounce-back) make it easy for the LB method to treat complex boundary conditions in pore structures. The simple implementation and high parallelism of the LB method further enhance its computational efficiency, making it well-suited for pore-scale simulations. Accordingly, there exist plentiful LB models for independent investigations of the multiple physics behind CO_2 desublimation in a contact liquid, including two-phase flow, multicomponent transport, conjugate heat transfer, homogeneous and heterogeneous solidification, and solid structure evolutions. For instance, LB models were proposed for simulating two-phase flows at the pore scale, where the multiple-relaxation-time (MRT) scheme and the multiple distribution functions were incorporated to improve the model stability and consider the multicomponent transport, respectively (Li et al., 2016; Wang et al., 2022; 2023). The feasibility of LB model was also verified in simulating species transport across gas–liquid interfaces, with the mass jump described by Henry's law. This mass jump was successfully implemented by incorporating either the continuum species transport source term or the boundary scheme in LB simulations (Chen et al., 2020; Yang et al., 2022). In the LB community, the conjugate heat transfer across different phases could be solved without resorting to conventional extrapolations or iterations (He et al., 2019). A half-lattice division scheme was proposed to model the conjugate heat transfer, but it was limited to cases with steady-state solutions or uniform heat capacities (Wang et al., 2007; Wang and Pan, 2008). Considering this, a new source term derived from the energy conservation equation was introduced in LB equations to realize the conjugate heat transfer during coke combustion and methane hydrate dissolution (Karani and Huber, 2015; Lei et al., 2021; Zhang et al., 2019). Finally, the homogeneous CO_2 desublimation in the contact liquid can be described by the classical nucleation theory, while the heterogeneous CO_2 desublimation on solid CO_2 surfaces can be treated by boundary conditions for mass conservation and conjugate heat transfer (Jensen, 2015; Lei et al., 2023; 2024). In applications like salt precipitation and CO_2 sequestration, the homogeneous nucleation in the liquid phase was successfully solved by introducing source terms in LB simulations (Chen et al., 2014; Yang et al., 2023). To enforce the heterogeneous solidification on solid surfaces, a general bounce-back scheme was built to treat the mass conservation condition, which displayed the second-order accuracy at complex boundaries (Zhang et al., 2012). Along with these solidification simulations, the volume of pixel (VOP) scheme coupled with the mass balance equation was applied to explicitly track the pore-scale solid structure evolutions (Chen et al., 2014; Kang et al., 2006).

In general, separate LB models are available for individually modeling the key physics behind CO_2 desublimation in a contact liquid at the pore scale. However, the combination and interactions of these complex physics have not been achieved by a single LB model, which is indeed changeling. In our recent studies, an LB model has been proposed to simulate CO_2 desublimation on solid surfaces. This model successfully reproduced CO_2 desublimation properties under various conditions and identified different desublimation regimes (Lei et al., 2023, Lei et al., 2024). Nevertheless, the presence of contact liquid was not considered, thus neglecting the two-phase flow, transport of CO_2 between the gas and liquid phases, homogeneous CO_2 desublimation in the liquid phase, and temperature variations across three phases. To fill these gaps, this study aims to extend our recently proposed LB model to investigate CO_2 desublimation in a contact liquid during CCC at the pore level, accounting for the multiphysics involved and their interactions. The CO_2 capture performance of liquid-based CCC will be evaluated for different operating parameters, which are expected to elucidate the optimal conditions and enhance the understanding of CCC.

2. Mathematical and physical models

This study investigates the multiphysics behind CO_2 desublimation in a contact liquid during CCC. Fig. 1 depicts a sample desublimation column filled with contact liquid (Fazlollahi et al., 2017). From the inlet, an incompressible warm flue gas containing CO_2 and N_2, with mass fractions Y_0 and $(1 - Y_0)$ respectively, is injected at temperature T_0, pressure p_0, and velocity $\boldsymbol{u}_0$. Initially, the temperature of the contact liquid (T_l)

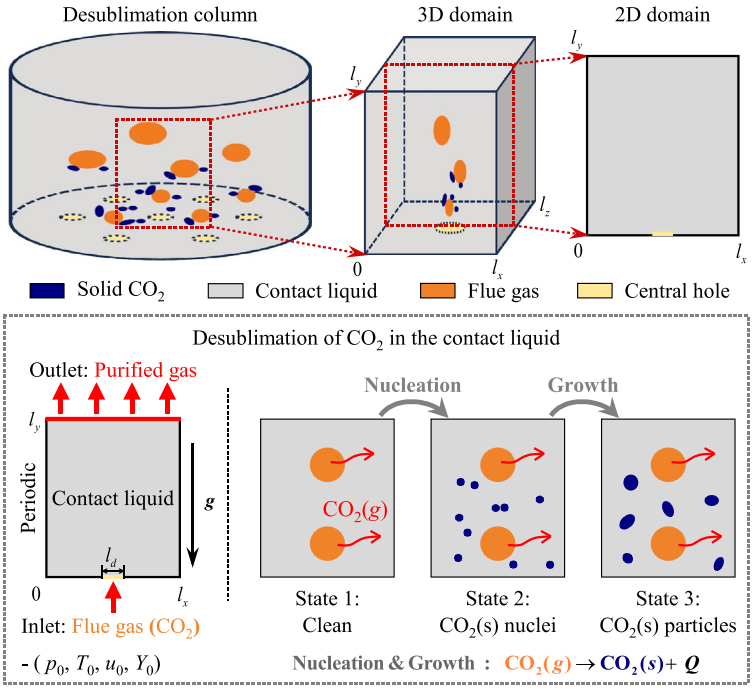

Fig. 1. The schematic diagram of CO_2 desublimation in a contact liquid at the pore scale.

is set above the freezing point of N_2 but below that of CO_2. As a result, N_2 exits the domain without undergoing phase change, but CO_2 desublimates and remains within the liquid. Specifically, the CO_2 component diffuses across the gas–liquid interface and desublimates to form solid CO_2 nuclei in the contact liquid. As CO_2 desublimation continues both in the liquid and on solid CO_2 surfaces, CO_2 nuclei gradually grow into large solid CO_2 particles. The generation of solid CO_2 particles affects the two-phase flow (i.e., the flue gas and contact liquid) in the desublimation column. The modified two-phase convection and gas–liquid interfaces impact the transport of CO_2 component. Meanwhile, considering the exothermic nature of desublimation and the incoming warm flue gas, the local temperature gradually increases with conjugate heat transfer through different phases. The variations in CO_2 mass fraction and temperature in turn influence the CO_2 desublimation rate. Therefore, the underlying physics of CO_2 desublimation, namely, the two-phase flow, heat and mass transfer, CO_2 desublimation mechanisms, and solid CO_2 structure evolution, are fully coupled.

Before constructing governing equations for describing desublimation of CO_2 at the pore scale, some simplifications and assumptions are made as follows. (1) The capture (or desublimation) of CO_2 is investigated, while the cooling of the system and the recovery of the desublimated CO_2 are neglected. (2) The incompressible flue gas obeys the ideal gas law, and it is represented as a mixture of CO_2 and N_2. (3) Fick's law is applied to describe the mass diffusion of gas components in both the gas and liquid phases, and the mass jump across gas–liquid interfaces is determined by Henry's law. (4) The desublimation of CO_2 is simplified into two steps: nucleation and growth. The homogeneous desublimation (i.e., nucleation) within the contact liquid follows the classical nucleation theory, while the heterogeneous desublimation (i.e., growth) on solid CO_2 surfaces is determined by the local deviation from the gas/liquid–solid equilibrium state. (5) Thermophysical properties of the gas, liquid, and solid phases are set as constants in relation to the initial condition. (6) The movement of solid CO_2 is not considered.

Based on the aforementioned assumptions and introductions, a set of governing equations has been developed to model the desublimation of CO_2 during CCC at the pore scale. This includes the continuity Eq. (1), the incompressible Navier–Stokes Eq. (2), the conservation Allen–Cahn Eq. (3) for the two-phase flow, the species conservation Eq. (4) for CO_2 transport in the gas and liquid phases, and the energy balance Eq. (5) for heat transfer through the gas, liquid, and solid phases (Lei et al., 2023; Liang et al., 2018; Yang et al., 2023).

$$\nabla \cdot (\rho \boldsymbol{u}) = 0, \tag{1}$$

$$\frac{\partial(\rho \boldsymbol{u})}{\partial t} + \nabla \cdot (\rho \boldsymbol{u}\boldsymbol{u}) = -\nabla p + \nabla \cdot \left[\rho\nu\left(\nabla \boldsymbol{u} + (\nabla \boldsymbol{u})^T\right)\right] + \boldsymbol{F}_s + \boldsymbol{F}_g, \tag{2}$$

$$\frac{\partial \phi}{\partial t} + \nabla \cdot (\phi \boldsymbol{u}) = \nabla \cdot [M(\nabla \phi - \lambda \boldsymbol{n})], \tag{3}$$

$$\frac{\partial Y}{\partial t} + \nabla \cdot (Y\boldsymbol{u}) = \nabla \cdot \left[D\left(\nabla Y + \Phi_{CST}\right)\right] + S_n,$$
$$\Phi_{CST} = -\frac{Y(H-1)}{H\phi + (1-\phi)}\nabla \phi, \tag{4}$$

$$\frac{\partial\left(\rho c_p T\right)}{\partial t} + \nabla \cdot \left(\rho c_p T \boldsymbol{u}\right) = \nabla \cdot \left(\rho c_p \alpha \nabla T\right) + Q. \tag{5}$$

Here, $\boldsymbol{u}$, ρ, and ν represent fluid velocity, density, and kinematic viscosity, respectively. t is time. ϕ is the phase indicator, with $\phi = 0.0$ for gas, $\phi = 1.0$ for liquid, and $\phi = 0.5$ for the gas–liquid interface. The unit vector normal to the interface is calculated by,

$$\boldsymbol{n} = \frac{\nabla \phi}{|\nabla \phi|}. \tag{6}$$

M denotes mobility, and λ is a function of ϕ as,

$$\lambda = \frac{4\phi(1-\phi)}{W}, \tag{7}$$

with W representing the gas–liquid interface thickness. The volumetric body force $\boldsymbol{F}_g = \left(\rho - \rho_l\right)\boldsymbol{g}$ is imposed on the system, with ρ_l being the liquid density and $\boldsymbol{g}$ being the gravitational acceleration. One of the widely used potential forms in the phase-field method is applied to determine the surface tension force $\boldsymbol{F}_s$ as,

$$\boldsymbol{F}_s = \mu_\phi \nabla \phi. \tag{8}$$

The chemical potential μ_ϕ is defined as,

$$\mu_\phi = 4\beta\phi(\phi-1)(\phi-0.5) - \kappa\nabla^2\phi, \tag{9}$$

where $\kappa = 3\sigma W/2$, $\beta = 12\sigma/W$, and σ is the surface tension.

In the mass and energy conservation Eqs. (4)–(5), Y and D are the CO_2 mass fraction and diffusion coefficient, respectively. S_n is the source term caused by homogeneous desublimation of CO_2, and Φ_{CST} is the source term for CO_2 mass jump at the gas–liquid interface. Such a mass jump is described by $Y_l = HY_g$, with H being the Henry coefficient, and Y_l and Y_g representing the CO_2 mass fractions in the liquid and gas phases, respectively. T is the local temperature, c_p is the specific heat capacity at constant pressure, α is the thermal diffusivity, and Q is the heat released from CO_2 desublimation.

As shown in Fig. 1, the exothermic CO_2 desublimation is expressed as,

$$CO_2(g) \rightarrow CO_2(s) + Q. \tag{10}$$

Here, the gas and solid phases of CO_2 are denoted by g and s, respectively. The liquid is gradually warmed up by the exothermic desublimation process and the incoming warm gas. Once the local temperature reaches the freezing point of CO_2, the desublimation of CO_2 stops. From such a desublimation process, the released heat Q is calculated as,

$$Q = m_r a_r h_r, \tag{11}$$

with h_r being the enthalpy change of CO_2 desublimation and a_r being the specific surface area per unit volume. Considering that CO_2 desublimates into solid through either the homogeneous nucleation within the contact liquid or the heterogeneous solidification on solid CO_2 surfaces, the mass transfer rate m_r is calculated as (Debnath et al., 2019; Lei et al., 2023; Yang et al., 2023),

$$m_r = \begin{cases} k_n \exp\left(\Delta G / k_B T\right), & \text{in the contact liquid,} \\ k_r\left(y_i p - p_e\right), & \text{on solid } CO_2 \text{ surfaces.} \end{cases} \tag{12}$$

Here, k_n and k_r are mass desublimation rate constants, ΔG is the Gibbs free energy, k_B is the Boltzmann constant, and y_i is the CO_2 mole fraction. The gas/liquid–solid equilibrium pressure is estimated as (Tuinier et al., 2010),

$$p_e = \exp\left(10.257 - \frac{3082.7}{T} + 4.08 \ln T - 2.2658 \times 10^{-2} T\right). \tag{13}$$

Based on the mass transfer rate in (12), the nucleation source term is $S_n = Y m_r$. During CO_2 desublimation, the structure of solid CO_2 is tracked by the mass balance equation (Kang et al., 2014),

$$\rho_s \partial_t V_s = m_r a_r V_r, \tag{14}$$

where V_s and ρ_s represent the volume and density of solid CO_2, respectively, and V_r is the active volume for desublimation.

To solve the above governing equations, boundary conditions at both internal and external boundaries of the computational domain are introduced. On the one hand, external boundary conditions are set as follows. First, from the inlet ($y = 0$), the flue gas is injected into the domain at a given operating condition. Accordingly, the gas compositions, temperature, pressure, and velocity are set as specified values. Then, at the outlet ($y = l_y$), a fully developed flow is considered and the zero-gradient velocity and the no-flux temperature and mass fraction are applied. Finally, the periodic conditions are imposed at the lateral sides ($x = 0,\ l_x$ and $z = 0,\ l_z$). On the other hand, the desublimation of CO_2 takes place on solid CO_2 surfaces (I). Such internal boundary conditions are described by,

$$\text{No-slip velocity: } \boldsymbol{u}^I = (0,\ 0), \tag{15}$$

$$\text{Mass conservation: } \boldsymbol{n}^I \cdot D\rho\nabla Y^I = m_r, \tag{16}$$

Conjugate heat transfer:

$$\begin{cases} T^{I,+} = T^{I,-}, \\ \boldsymbol{n}^I \cdot \left(k\nabla T + \rho c_p \boldsymbol{u} T\right)^{I,+} = \boldsymbol{n}^I \cdot \left(k\nabla T + \rho c_p \boldsymbol{u} T\right)^{I,-} + q. \end{cases} \tag{17}$$

In the above equations, $\boldsymbol{n}^I$ is the surface normal pointing to the gas or liquid phase, $+$ and - denote parameters on either side of I, $k = \alpha \rho c_p$ is the thermal conductivity, and q is the heat flux caused by CO_2 desublimation. Once the local temperature increases to the freezing point of solid CO_2, the desublimation of CO_2 stops with $m_r = 0$ and $q = 0$. Thus, the no-slip and no-flux boundary conditions are implemented.

In order to model CO_2 desublimation using the LB method, the above physical parameters should be converted to those in lattice units. For this purpose, dimensionless parameters are derived to act as the conversion criterions between the two systems of units. By introducing the characteristic length L, velocity U, and temperature T_{ch}, dimensionless parameters marked by asterisks are derived as,

$$\begin{aligned} &\boldsymbol{x}^* = \frac{\boldsymbol{u}}{L},\ t^* = \frac{t}{L/U},\ \boldsymbol{u}^* = \frac{\boldsymbol{u}}{U},\ \rho^* = \frac{\rho}{\rho_g},\ p^* = \frac{p}{\rho_g U^2},\ T^* = \frac{T}{T_{ch}}, \\ &m_r^* = \frac{m_r}{\rho_g U},\ h_r^* = \frac{h_r}{c_{p,g} T_{ch}},\ k_r^* = k_r U,\ \mathrm{Re} = \frac{LU}{\nu_g},\ \mathrm{Pe} = \frac{LU}{D_g},\ \mathrm{Pr} = \frac{\nu}{\alpha_g}. \end{aligned} \tag{18}$$

The subscript g refers to physical properties of the flue gas. From such a dimensionless derivation, key characteristic numbers are obtained: the Reynolds number Re, the Péclet number Pe, and the Prandtl number Pr. In the following LB simulations, a match of these dimensionless variables ensures the same desublimation properties between the lattice space and the real physical coordinate.

3. Numerical method

A multiphysics LB model is built to solve the conservation Eqs. (1)–(5). Considering the varying thermophysical properties of gas, liquid, and solid phases, the energy conservation Eq. (5) is recast as (Lei et al., 2021),

$$\begin{aligned} &\partial_t T + \nabla \cdot (T\boldsymbol{u}) = \nabla \cdot (\alpha \nabla T) + F_t, \\ &F_t = \frac{Q}{\rho c_p} + \frac{\nabla\left(\rho c_p\right) \cdot (\alpha \nabla T - T\boldsymbol{u})}{\rho c_p} - \frac{T \partial_t\left(\rho c_p\right)}{\rho c_p}, \end{aligned} \tag{19}$$

with F_t being the new source term.

To solve the two-phase flow (Eqs. (1)–(3)), species transport (Eq. (4)), and heat transfer (Eq. (19)), four sets of LB evolution equations are built as follows (Guo and Shu, 2013; Lei et al., 2023; Liang et al., 2018; Yang et al., 2023),

$$\begin{aligned} &f_i\left(\boldsymbol{x} + \boldsymbol{e}_i \delta_t,\ t + \delta_t\right) - f_i(\boldsymbol{x},\ t) \\ &\quad = -\left(\boldsymbol{M}^{-1} \boldsymbol{S} \boldsymbol{M}\right)_{ij} \left[f_j(\boldsymbol{x},\ t) - f_j^{eq}(\boldsymbol{x},\ t)\right] + \delta_t F_i, \end{aligned} \tag{20}$$

$$\begin{aligned} &p_i\left(\boldsymbol{x} + \boldsymbol{e}_i \delta_t,\ t + \delta_t\right) - p_i(\boldsymbol{x},\ t) \\ &\quad = -\left(\boldsymbol{M}^{-1} \boldsymbol{S}_\phi \boldsymbol{M}\right)_{ij} \left[p_j(\boldsymbol{x},\ t) - p_j^{eq}(\boldsymbol{x},\ t)\right] + \delta_t F_{p,i}, \end{aligned} \tag{21}$$

$$\begin{aligned} &g_i\left(\boldsymbol{x} + \boldsymbol{e}_i \delta_t,\ t + \delta_t\right) - g_i(\boldsymbol{x},\ t) \\ &\quad = -\left(\boldsymbol{M}^{-1} \boldsymbol{S}_y \boldsymbol{M}\right)_{ij} \left[g_j(\boldsymbol{x},\ t) - g_j^{eq}(\boldsymbol{x},\ t)\right] + \delta_t F_{y,i}, \end{aligned} \tag{22}$$

$$\begin{aligned} &h_i\left(\boldsymbol{x} + \boldsymbol{e}_i \delta_t,\ t + \delta_t\right) - h_i(\boldsymbol{x},\ t) \\ &\quad = -\left(\boldsymbol{M}^{-1} \boldsymbol{S}_t \boldsymbol{M}\right)_{ij} \left[h_j(\boldsymbol{x},\ t) - h_j^{eq}(\boldsymbol{x},\ t)\right] + \delta_t F_{t,i}, \end{aligned} \tag{23}$$

where i and j are discrete directions. For fluid moving with discrete velocity $\boldsymbol{e}_i$ at position $\boldsymbol{x}$ and time t, $f_i(\boldsymbol{x},\ t)$, $p_i(\boldsymbol{x},\ t)$, $g_i(\boldsymbol{x}, t)$, and $h_i(\boldsymbol{x}, t)$ are distribution functions for the hydrodynamics, phase indicator, CO_2 mass fraction, and temperature fields, respectively. The equilibrium distribution functions are given as Lei et al. (2023), Liang et al. (2018),

$$f_i^{eq} = \begin{cases} \frac{p}{c_s^2}\left(w_i - 1\right) + \rho s_i, & i = 0, \\ \frac{p}{c_s^2} w_i + \rho s_i, & i \neq 0, \end{cases}$$

$$\text{with } s_i = w_i \left(\frac{\boldsymbol{e}_i \cdot \boldsymbol{u}}{c_s^2} + \frac{\left(\boldsymbol{e}_i \cdot \boldsymbol{u}\right)^2}{2c_s^4} - \frac{\boldsymbol{u}^2}{2c_s^2} \right). \tag{24}$$

$$p_i^{eq} = w_i\phi\left(1+\frac{\boldsymbol{e}_i\cdot\boldsymbol{u}}{c_s^2}\right), \tag{25}$$

$$g_i^{eq} = w_i Y\left[1+\frac{\boldsymbol{e}_i\cdot\boldsymbol{u}}{c_s^2}+\frac{(\boldsymbol{e}_i\cdot\boldsymbol{u})^2}{2c_s^4}-\frac{\boldsymbol{u}^2}{2c_s^2}\right], \tag{26}$$

$$h_i^{eq} = w_i T\left[1+\frac{\boldsymbol{e}_i\cdot\boldsymbol{u}}{c_s^2}+\frac{(\boldsymbol{e}_i\cdot\boldsymbol{u})^2}{2c_s^4}-\frac{\boldsymbol{u}^2}{2c_s^2}\right]. \tag{27}$$

Here, $c_s = e/\sqrt{3}$ is the lattice sound velocity and e is the lattice speed. $\boldsymbol{S}$, $\boldsymbol{S}_\phi$, $\boldsymbol{S}_y$, and $\boldsymbol{S}_t$ are diagonal relaxation matrices. $\boldsymbol{M}$ is the transformation matrix to map distribution functions from the physical space to the moment space. The distribution functions for source terms are (Lei et al., 2023; Liang et al., 2018; Yang et al., 2022),

$$F_i = w_i\left(1-\frac{1}{2\tau}\right)\left[\boldsymbol{u}\cdot\nabla\rho+\frac{\boldsymbol{e}_i\cdot(\boldsymbol{F}_s+\boldsymbol{F}_g)}{c_s^2}+\frac{\boldsymbol{u}\nabla\rho:(\boldsymbol{e}_i\boldsymbol{e}_i-c_s^2\boldsymbol{I})}{c_s^2}\right], \tag{28}$$

$$F_{p,i} = w_i\left(1-\frac{1}{2\tau_p}\right)\frac{\boldsymbol{e}_i\cdot\left[\partial_t(\phi\boldsymbol{u})+c_s^2\lambda\boldsymbol{n}\right]}{c_s^2}, \tag{29}$$

$$F_{y,i} = w_i\left(1-\frac{1}{2\tau_y}\right)\boldsymbol{e}_i\cdot\Phi_{CST}+w_i S_n, \tag{30}$$

$$F_{t,i} = w_i F_t, \tag{31}$$

with τ, τ_p, and τ_y being relaxation times. At each time step, after the above evolutions, the macroscopic variables are calculated as (Lei et al., 2023; Liang et al., 2018),

$$\begin{aligned} &p = \frac{c_s^2}{1-w_0}\left[\sum_{i\neq 0} f_i+\frac{\delta t}{2}\boldsymbol{u}\cdot\nabla\rho+\rho s_0\right], \quad \rho\boldsymbol{u} = \sum_i \boldsymbol{e}_i f_i+\frac{\delta t}{2}(\boldsymbol{F}_s+\boldsymbol{F}_g),\\ &\phi = \sum_i p_i, \quad Y = \sum_i g_i, \quad T = \sum_i h_i. \end{aligned} \tag{32}$$

To enforce the CO_2 desublimation on solid CO_2 surfaces I, LB boundary schemes are developed. The no-slip velocity in Eq. (15) is addressed by the halfway bounce-back scheme and the conjugate heat transfer in Eq. (17) is implemented by solving the energy conservation Eq. (19). As for the mass conservation condition in Eq. (16), the surface mass fraction gradient ∇Y^I is calculated based on the finite-difference scheme as (Zhang et al., 2012),

$$\boldsymbol{n}^I\cdot\nabla Y^I = \frac{Y-Y^I}{0.5\boldsymbol{n}\cdot\boldsymbol{e}_i\delta_x}, \tag{33}$$

where Y is the CO_2 mass fraction at the gas or liquid grid neighboring I. By inserting Eq. (33) into Eq. (16) and using the ideal gas law, the value of Y^I is calculate as,

$$Y^I = \frac{D\rho Y+0.5\boldsymbol{n}\cdot\boldsymbol{e}_i\delta_x k_r p_e}{D\rho+0.5\boldsymbol{n}\cdot\boldsymbol{e}_i\delta_x k_r p_0 T/T_0}. \tag{34}$$

The mass conservation boundary is thus deduced into a boundary with a given mass fraction Y^I, implemented using the halfway bounce-back scheme (Lei et al., 2023).

Furthermore, the VOP method is adopted to treat the evolution of solid CO_2 in Eq. (14) (Kang et al., 2006; Wang et al., 2019). Explicitly, a fine enough mesh is applied to cover the computational domain. Thus, each grid represents only one material: solid CO_2, flue gas, or contact liquid. Each grid node is located at the center of a unit volume. Initially, the volume of solid CO_2 is set as $V_s = 0$ for gas and liquid grids. As CO_2 desublimation happens, the value of V_s is updated at each time step by,

$$V_s(t+\delta_t) = V_s(t)+m_r a_r V_r/\rho_s. \tag{35}$$

As V_s increases to $V_s = 1$ at a liquid or gas grid, this grid transforms into a solid CO_2 grid. Then, when V_s doubles to $V_s = 2$ at a solid CO_2 grid, one of its neighboring gas or liquid grids expands into a solid CO_2 grid. After model validations, the developed multiphysics LB model is applied to investigate CO_2 desublimation within a contact liquid at the pore scale. More details about the proposed LB model are provided in Appendices Appendix A–Appendix B.

Table 1
Parameters for pore-scale simulations of CO_2 desublimation in a contact liquid.

Physical properties	Values
Contact liquid temperature, T_l	[135, 160] K
Flue gas temperature, T_0	[165, 250] K
CO_2 mass fraction, Y_0	[0.1, 1.0]
Flue gas injection velocity, Pe	[1.4, 14]
CO_2 diffusion coefficient in gas, D_g	1.63×10^{-5} m^2/s
CO_2 diffusion coefficient in liquid, D_l	2.91×10^{-9} m^2/s
Flue gas density, ρ_g	1.46kg/m^3
Flue gas specific heat capacity, $c_{p,g}$	0.846 kJ/kgK
Flue gas thermal diffusivity, α_g	5.02×10^{-6} m^2/s
Flue gas kinematic viscosity, ν_g	1.01×10^{-5} m^2/s
Contact liquid density, ρ_l	620 kg/m^3
Contact liquid specific heat capacity, $c_{p,l}$	2.25 kJ/kgK
Contact liquid thermal diffusivity, α_l	9.10×10^{-8} m^2/s
Contact liquid kinematic viscosity, ν_l	3.55×10^{-7} m^2/s
Solid CO_2 density, ρ_s	1.56×10^3 kg/m^3
Solid CO_2 specific heat capacity, $c_{p,s}$	0.967 kJ/kgK
Solid CO_2 thermal diffusivity, α_s	4.64×10^{-7} m^2/s
Mass desublimation rate constant, k_n	10^{-6} kgm/s
Mass desublimation rate constant, k_r	10^{-6} s/m
Enthalpy change of desublimation, h_r	5.682×10^5 J/kg

Compared to our recent model for simulating CO_2 desublimation on solid surfaces (Lei et al., 2023), the current multiphysics LB model extends to include the contact liquid. The mathematical and numerical models developed here are advanced by incorporating two-phase flow, both homogeneous and heterogeneous CO_2 desublimation, CO_2 transport between air and liquid phases, and temperature transfer across all three phases. These newly integrated physical processes cover the limitations of our recent model, thereby allowing for a comprehensive treatment of the multiphysics involved in liquid-based CCC.

4. Results and discussion

For the desublimation system in Fig. 1, key geometrical parameters are set as: length $l_x = 43$ cm, height $l_y = 50$ cm, width $l_y = 43$ cm, and central hole diameter $l_d = 2$ cm. Initially, the system is filled by a contact liquid at T_l and the incompressible flue gas at (T_0, Y_0, u_0, p_0) is injected from the inlet. Considering that T_l is lower than the freezing point of CO_2, the CO_2 component desublimates and remains within the liquid for collection. In the subsequent simulations, desublimation parameters and thermalphysical properties are set as listed in Table 1. These physical parameters can be converted into lattice units based on a match of dimensionless parameters in Eq. (18), where characteristic parameters are,

$$L = l_y, \quad U = u_0, \quad T_{ch} = 175 \text{ K}. \tag{36}$$

Prior studies have emphasized the importance of the liquid temperature T_l, gas temperature T_0, CO_2 mass fraction Y_0, and gas injection velocity u_0 to the carbon capture performance of CCC (Fazlollahi et al., 2017; Jensen, 2015; Lei et al., 2023). Therefore, operating conditions are evaluated for ranges of these parameters as listed in Table 1. Note that, the gas injection velocity u_0 is characterized by the dimensionless Péclet number Pe. The contact liquid is set as isopentane in the present study and can be substituted with other suitable cryogenic liquids by adjusting the corresponding physical properties in future work. In this study, a mesh of size $256\times300\times256$ is selected to describe the 3D desublimation domain in Fig. 1. From this 3D domain, an xy cross-section at $z = 0.5l_z$ is selected for 2D simulations and the mesh size is 256×300. Each simulation test continues until the CO_2 content in the outflow flue gas reaches the termination condition of $Y = 0.1Y_0$. The duration of the desublimation process until the termination point is termed as the operation time period t_e.

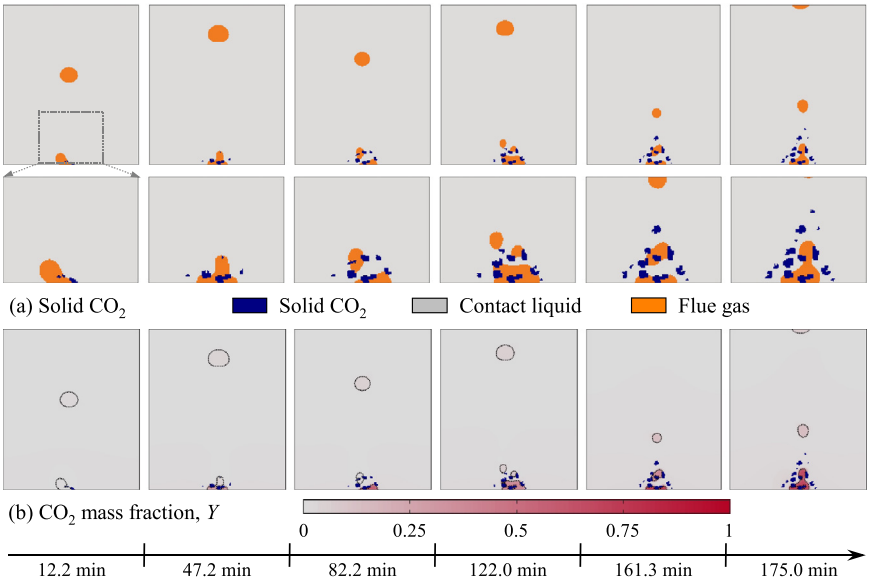

Fig. 2. CO_2 desublimation in a contact liquid at $T_l = 145$ K, $T_0 = 175$ K, $Y_0 = 1.0$, and Pe = 1.4. Contours of (a) solid CO_2 and (b) CO_2 mass fraction Y at six time instants $t = 12.2, 47.2, 82.6, 122.0, 161.3, 175.0$ min.

4.1. CO_2 Desublimation properties

The initial objective is to investigate CO_2 desublimation properties in a contact liquid. A 2D test with the liquid temperature $T_l = 145$ K, flue gas temperature $T_0 = 175$ K, CO_2 mass fraction $Y_0 = 1.0$, and Péclet number Pe = 1.4 (or gas injection velocity) is simulated. The obtained evolutions of solid CO_2 and CO_2 mass fraction Y over time are illustrated in Fig. 2.

The growth and distribution of solid CO_2 in a contact liquid are displayed over time in Fig. 2(a). At 12.2 min, small solid CO_2 nuclei are visible. This occurs because, after injection, the CO_2 component from flue gas diffuses across the gas–liquid interfaces and enters the contact liquid, where the homogeneous CO_2 desublimation takes place and produces solid CO_2 nuclei. These nuclei gradually grow and show a pronounced presence of solid CO_2 particles by 47.2 min. After that, the solid CO_2 regions further expand and become prominent, indicating the continued CO_2 desublimation process. Finally, from 161.3 min to 175.0 min, the expansion of solid CO_2 areas slows down, highlighting the decreased CO_2 desublimation rate over the period. Fig. 2(b) depicts contours of CO_2 mass fraction (Y) at varying time instants, where the gas–liquid interfaces are indicated by dashed lines. At 12.2 min, Y is uniformly low, indicating that the injected CO_2 component efficiently diffuses into the contact liquid and undergoes desublimation at this early stage. By 82.2 min, there is a noticeable increase in Y around the solid CO_2 areas. This stems from the fact that the continuous CO_2 desublimation increases the local temperature and reduces the available sites for further desublimation. As a result, near the solid CO_2 areas, the CO_2 desublimation rate slows down and the consumption of the CO_2 component diminishes. Correspondingly, the diffusion of CO_2 from the gas phase to the liquid phase becomes degraded and Y within the gas phase is amplified in those areas. Following the continuous decrease in the CO_2 desublimation rate, Y steadily increases and spreads, particularly within the gas phases around the solid CO_2 regions.

For comparison, the above case is repeated with CO_2 desublimation turned off. Distributions of solid CO_2 and CO_2 mass fraction Y at six time instants are illustrated in Fig. 3. As expected, no solid CO_2 is generated in this case due to the absence of CO_2 desublimation. Meanwhile, Fig. 3(b) shows that Y is consistently high in the gas phase but significantly lower in the liquid phase. This is attributed to the slow CO_2 diffusion from the flue gas to the contact liquid as well as the CO_2 mass fraction drop at the gas–liquid interfaces. These results differ significantly from those in Fig. 2, demonstrating that the existence of CO_2 desublimation can effectively capture CO_2 from the flue gas.

To quantify the CO_2 capture capacity of the contact liquid, the volume fraction of solid CO_2 captured (ϕ_c) is calculated by,

$$\phi_c = \frac{1}{l_x l_y}\int_0^{l_x}\int_0^{l_y} V_s(x,y)\,dy\,dx \times 100\%. \tag{37}$$

Furthermore, considering the crucial role of monitoring the termination of the desublimation process, the CO_2 content in the outgoing gas phase (η_o) is estimated as,

$$\eta_o = \frac{1}{l_{x,g} Y_0}\int_0^{l_{x,g}} Y\left(x, l_y\right)dx \times 100\%, \tag{38}$$

where $l_{x,g}$ is the length occupied by the flue gas at the outlet. As introduced above, each simulation test stops once η_o reaches 10%. The calculated values of ϕ_c and η_o are plotted against time in Fig. 4(a)–(b). These plots are explained using the averaged temperature ($\overline{T}$) and the overall desublimation rate (m_r^*), as shown in Fig. 4(c)–(d). Here $\overline{T}$ is defined as the averaged temperature over the entire computational domain,

$$\overline{T} = \frac{1}{l_x l_y}\int_0^{l_x}\int_0^{l_y} T(x,y)\,dy\,dx. \tag{39}$$

The overall desublimation rate m_r^* is calculated as,

$$m_r^* = \frac{1}{\rho_g u_0}\int_0^{l_x}\int_0^{l_y} m_r(x,y)\,dy\,dx. \tag{40}$$

In Fig. 4(a), the volume fraction of solid CO_2 captured (ϕ_c) is plotted over time. The black line represents the scenario with CO_2 desublimation, showing a steady increase in the value of ϕ_c. This indicates the continuous CO_2 desublimation process within the contact liquid. Insets within the plot illustrate the morphological evolutions of solid CO_2 captured. The growth rate of ϕ_c is observed to decline over time, which corresponds to the decreasing desublimation rate m_r^* in Fig. 4(d). This decline is driven by the rising temperature $\overline{T}$ in Fig. 4(c), which slows down the CO_2 desublimation intensity (m_r^*) as described by Eq. (40). Fig. 4(b) depicts the outgoing CO_2 content in the flue gas (η_o). The case with CO_2 desublimation exhibits a relatively low level of η_o (i.e., $\eta_o < 10\%$), suggesting the effective capture of the CO_2 component. In this scenario, η_o increases over time and its growth rate accelerates as time progresses. The rise in $\overline{T}$ and the decline in m_r^* are responsible for such an increasing trend in η_o. As the value of η_o increases to reach 10%, marked by the grey dash line in Fig. 4(b), the simulation arrives at its termination point. At this point, the maximum amount of solid CO_2 captured and the operation time period are recorded as ϕ_{cm} and t_e, respectively.

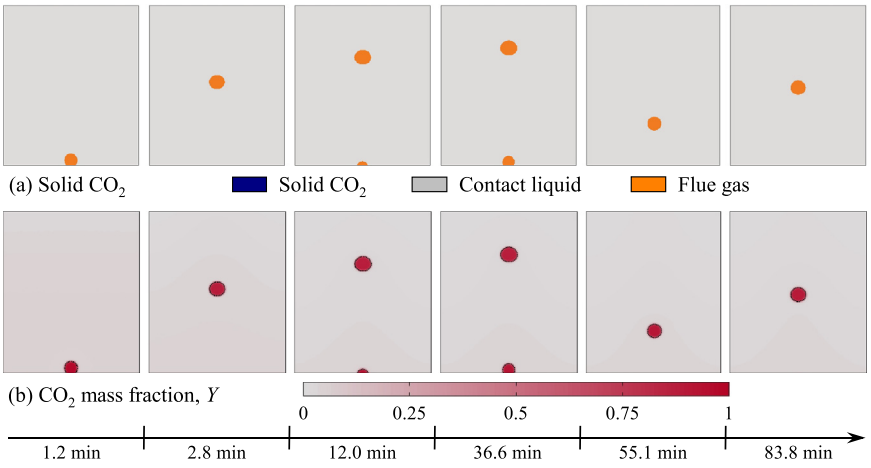

Fig. 3. CO_2 transport in a contact liquid without desublimation at T_l = 145 K, T_0 = 175 K, Y_0 = 1.0, and Pe = 1.4. Contours of (a) solid CO_2 and (b) CO_2 mass fraction Y at six time instants t = 1.2, 2.8, 12.0, 36.6, 55.1, 83.8 min.

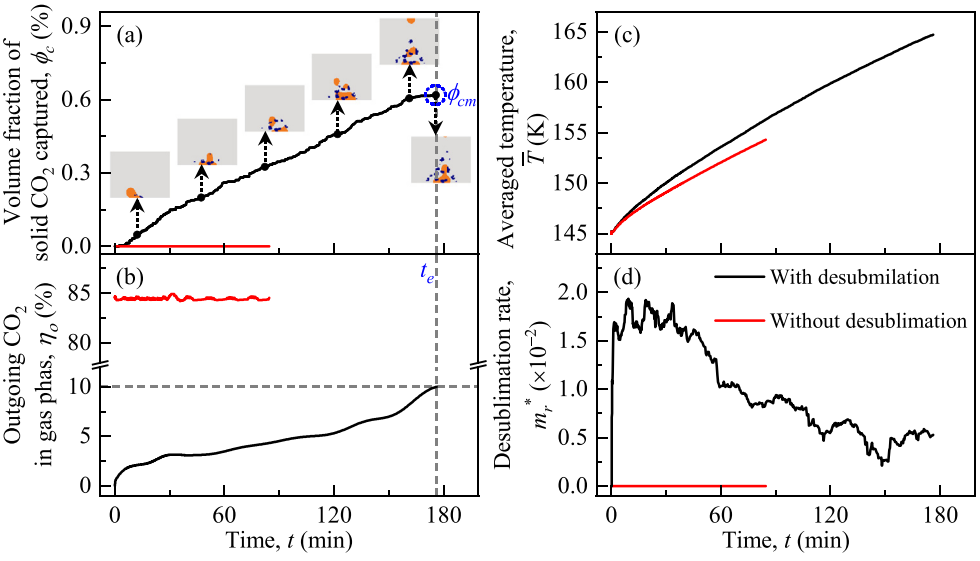

Fig. 4. Analyses of CO_2 desublimation in a contact liquid at T_l = 145 K, T_0 = 175 K, Y_0 = 1.0, and Pe = 1.4. Temporal evolutions of (a) volume fraction of solid CO_2 captured ϕ_c, (b) outgoing CO_2 content in the gas phase η_o, (c) averaged temperature $\overline{T}$, and (d) overall desublimation rate m_r^*.

For comparison, the scenario without CO_2 desublimation is represented by red lines in Fig. 4. In this case, ϕ_c remains zero and η_o stays at a high level (i.e. $\eta_o > 85\%$). It suggests that the injected CO_2 remains in the gas phase and exits the desublimation system without being captured as solid CO_2. Regarding the averaged temperature $\overline{T}$ shown in Fig. 4(c), it increases at a slower rate in the scenario without CO_2 desublimation compared to that with desublimation. This is because the heat released from CO_2 desublimation contributes to warming up the desublimation system. The comparison in Fig. 4 highlights the fact that CO_2 diffusion from the gas phase to the liquid phase is inadequate for flue gas purification. In contrast, CO_2 desublimation within the contact liquid can effectively capture the injected CO_2 component from the flue gas. Taken together, these quantitative analyses corroborate the above qualitative observations in Figs. 2–3 and provide insights into the CO_2 desublimation process within a contact liquid.

4.2. Comparison of 2D and 3D simulations

In the above 2D simulations, the generated solid CO_2 particles form porous structures within the contact liquid. Such structures potentially increase the active solid CO_2 surfaces for heterogeneous CO_2 desublimation but reduce the available liquid sites for homogeneous CO_2 nucleation. Additionally, the presence of solid CO_2 particles obstruct the movement of flue gas and hinder the transport of CO_2 component from the gas phase to the liquid phase, thereby impacting the CO_2 component available for desublimation. The complexities and effects of these porous solid CO_2 structures are expected to vary between 2D and 3D scenarios. Therefore, to verify the accuracy of 2D simulations, it is essential to investigate CO_2 desublimation within a contact liquid in three dimensions. The 3D simulation setup, shown in Fig. 1, mirrors the parameters used in Section 4.1 to ensure comparability.

Fig. 5 presents the results of 3D simulations of CO_2 desublimation in a contact liquid, conducted at the liquid temperature T_l = 145 K, flue gas temperature T_0 = 175 K, CO_2 mass fraction Y_0 = 1.0, and Péclet number Pe = 1.4 (or gas injection velocity). Fig. 5(a) displays 3D contours of solid CO_2 at various time instants, illustrating the nucleation and growth of solid CO_2 within the contact liquid. Initially, small solid CO_2 nuclei appear and progressively grow and merge into large porous structures, with the growth rate decreasing over time. An xy-plane view of the solid CO_2 distribution at $z = 0.5l_z$ is provided in Fig. 5(b). This perspective clearly depicts the progression from small and discrete solid CO_2 nuclei to large and interconnected solid CO_2 regions within the contact liquid. Fig. 5(c) illustrates distributions of the CO_2 mass fraction (Y) in the same xy-plane. At the early stage, the value of Y in the gas phase decreases significantly due to the desublimation of CO_2. Over time, however, it gradually increases since the CO_2 desublimation rate declines.

Temporal evolutions of the solid CO_2 captured (ϕ_c) and the outgoing CO_2 content in the gas phase (η_o) from 3D simulations are recorded in Fig. 6, which also includes results from 2D simulations for comparison. Note that, due to the 3D structure and the central hole, both ϕ_c and η_o

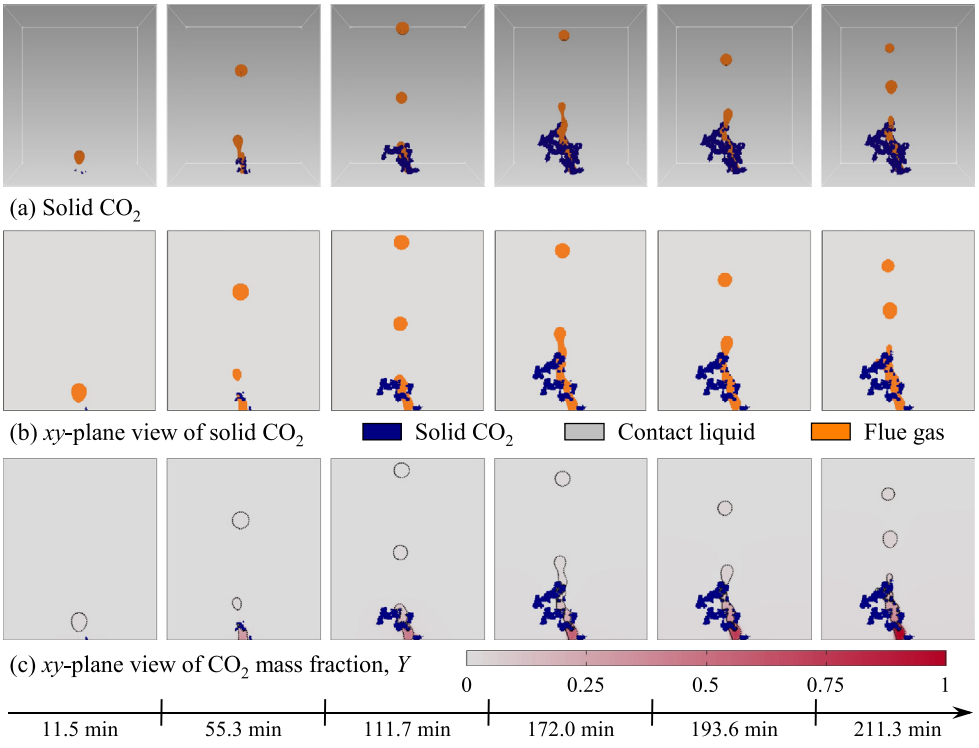

Fig. 5. 3D simulations of CO_2 desublimation in a contact liquid at T_l = 145 K, T_0 = 175 K, Y_0 = 1.0, and Pe = 1.4. Contours of (a) solid CO_2, (b) *xy*-plane view of solid CO_2 at $0.5l_z$, and (c) *xy*-plane view of CO_2 mass fraction Y at $0.5l_z$, for six time instants t = 11.5, 55.3, 111.7, 172.0, 193.6, 211.3 min.

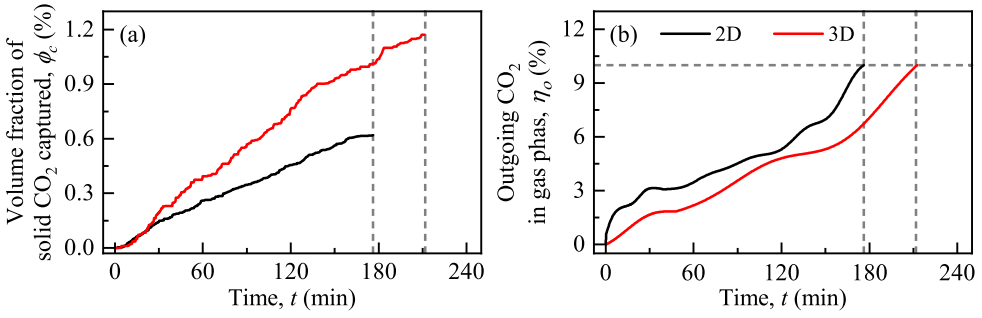

Fig. 6. Analyses of CO_2 desublimation in a contact liquid at T_l = 145 K, T_0 = 175 K, Y_0 = 1.0, and Pe = 1.4. Temporal evolutions of (a) volume fraction of solid CO_2 captured ϕ_c and (b) outgoing CO_2 content in the gas phase η_o.

in the 3D case are calculated as the average values of *xy*-planes ranging from $0.4l_z$ to $0.6l_z$. Fig. 6(a) shows that ϕ_c increases over time in both 2D and 3D simulations, implying the continuous CO_2 desublimation process. The 3D case consistently displays a higher ϕ_c compared to the 2D and thus the 3D model reproduces the more extensive desublimation of CO_2 in the contact liquid. This suggests that the additional z dimension allows for a more realistic representation of the CO_2 desublimation sites and their interactions, leading to a more effective description of the solid CO_2 generation in the contact liquid. The temporal evolution of η_o is provided in Fig. 6(b), demonstrating an increasing trend over time in both 2D and 3D simulations. Additionally, the 3D case continuously exhibits a lower η_o compared to the 2D one, which underscores the enhanced CO_2 capture efficiency through desublimation in three dimensions. This improved capture efficiency is attributed to the more realistic description of the complex solid CO_2 structures, species transport, and CO_2 desublimation processes in the 3D model.

Overall, compared to 2D studies, 3D simulations reveal the more intensive CO_2 desublimation dynamics and the higher CO_2 capture efficiency, stemming from the more realistic depiction of the porous CO_2 structures in three dimensions. Apart from these differences, CO_2 desublimation properties in the 3D case align well with the 2D results. It thus suggests that 2D simulations are sufficient for capturing the essential properties of CO_2 desublimation in a contact liquid. Moreover, 3D simulations are significantly more computationally demanding compared to 2D studies. For example, to simulate CO_2 desublimation in a contact liquid until the termination point, a 2D simulation requires 2.4 hours of parallel computation using 1280 computing cores, whereas a 3D simulation necessities 46.7 hours of computation using 20,480 cores. Therefore, 2D simulations provide a simple and computationally efficient approach while still delivering accurate insights into CO_2 desublimation behaviors in a contact liquid. The subsequent simulations will be conducted in two dimensions.

4.3. *Effects of operating conditions*

Following the discussion of CO_2 desublimation properties in a contact liquid, a parametric study is set out to examine the impacts of operating conditions, specifically the liquid temperature T_l, flue gas temperature T_0, CO_2 mass fraction Y_0, and gas injection velocity (or Pe), on the CO_2 capture performance. The CO_2 desublimation process is simulated across a range of these operating parameters as listed in Table 1. From simulations in Section 4.1, two key metrics emerge to quantify the CO_2 capture performance: the maximum volume fraction of solid CO_2 captured (ϕ_{cm}) and the operation time period for CO_2 desublimation (t_e). Using these two metrics, the CO_2 capture velocity is introduced as, $v_c = \phi_{cm}/t_e$. A higher v_c indicates a more efficient capture of CO_2, which is desirable.

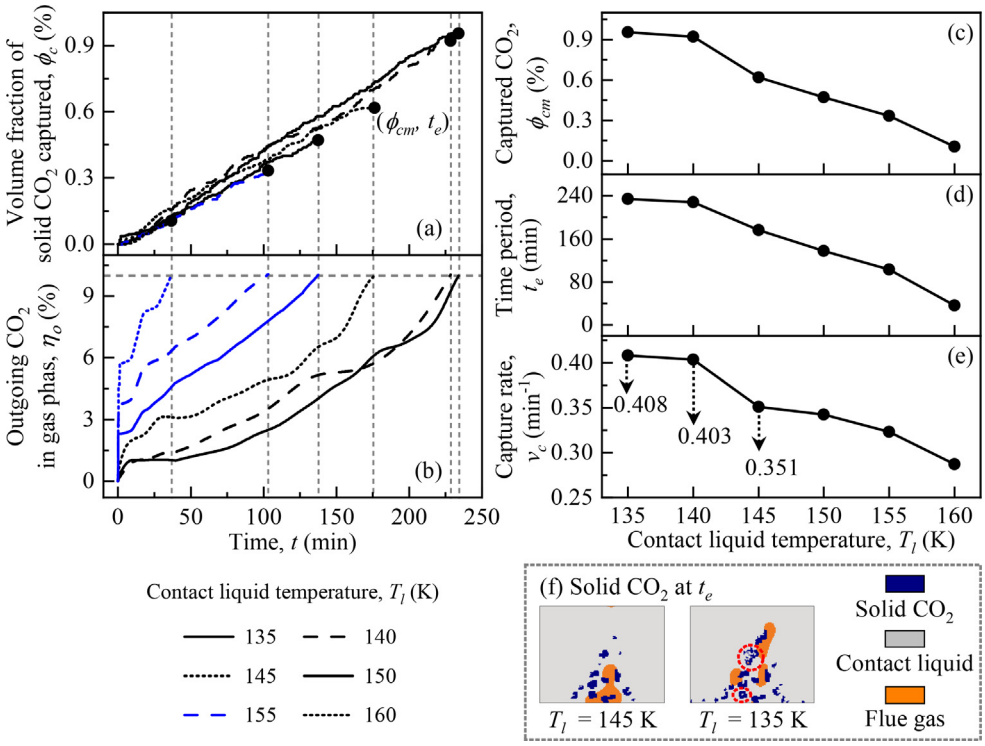

Fig. 7. Analyses of CO_2 capture performance in a contact liquid at $T_l \in [135,\ 160]$ K, T_0 = 175 K, Y_0 = 1.0, and Pe = 1.4. Temporal evolutions of (a) volume fraction of solid CO_2 captured ϕ_c and (b) outgoing CO_2 content in the gas phase η_o. (c) The maximum volume fraction of solid CO_2 captured ϕ_{cm}. (d) The operation time period for CO_2 desublimation t_e. (e) The CO_2 capture velocity v_c. (f) Distributions of solid CO_2 at t_e for simulations with T_l = 145 K and 135 K.

Fig. 7 illustrates the CO_2 capture performance in a contact liquid at various liquid temperatures T_l ranging from 135 K to 160 K, while keeping T_0 = 175 K, Y_0 = 1.0, and Pe = 1.4. Temporal evolutions of the volume fraction of solid CO_2 captured (ϕ_c) and the outgoing CO_2 content in the gas phase (η_o) are shown in Fig. 7(a)–(b). The simulation results exhibit a consistent CO_2 capture performance across all tested T_l values: both ϕ_c and η_o increase over time as the desublimation process continues. Additionally, a lower T_l slightly speeds up the growth in ϕ_c and significantly slows down the rise in η_o. It is because a colder contact liquid increases the CO_2 desublimation rate according to Eq. (12), thereby accelerating the consumption of CO_2 in both the liquid and gas phases. Under the fixed flues gas injection condition (i.e., fixed Y_0 and Pe), this subsequently leaves less CO_2 in the flue gas (η_o). Note that, regardless of the enhanced CO_2 desublimation rate, a lower T_0 speeds up the increase in ϕ_c only to a limited extent. This is because the injected CO_2 for desublimation is restricted by the given Y_0 and Pe. Based on profiles of ϕ_c and η_o in Fig. 7(a)–(b), the termination point (ϕ_{cm}, t_e) at η_o = 10 % is determined for each tested T_l. Results of ϕ_{cm} and t_e are plotted against T_l in Fig. 7(c)–(d). A clear trend stands out in these figures that, as T_l drops from 160 K to 135 K, both ϕ_{cm} and t_e increase obviously, albeit at a reduced rate. This trend is expected because a colder contact liquid decelerates the growth in η_o and thereby extends the CO_2 desublimation duration (t_e). Along with the intensified CO_2 desublimation rate, the low-T_l scenarios ultimately result in the amplified ϕ_{cm} and t_e.

To quantify the correlation between ϕ_{cm} and t_e, the CO_2 capture velocity $v_c = \phi_{cm}/t_e$ is calculated and illustrated in Fig. 7(e). The profile exhibits the successive growth in v_c following the descending T_l, which highlights the improved CO_2 capture efficiency. However, as T_l declines to an extremely low level, the increase in v_c becomes less pronounced. For example, the decrease in T_l from 145 K to 140 K yields the significant increase in v_c from 0.351 to 0.403, but further drops to 135 K only brings about a slight growth in v_c from 0.403 to 0.408. A likely factor is that, although the theoretical desublimate rate increases with the decreasing T_l, the CO_2 supply for desublimation remains nearly constant at the given Pe and Y_0. Correspondingly, at an extremely low T_l level (i.e., 135 K), the injected CO_2 becomes insufficient to satisfy the intensive desublimate rate, causing the system to transition from a CO_2-rich regime to a CO_2-limited regime. Another important factor is the fast CO_2 desublimation rate under low-T_l scenarios, which introduces the rapid generation of solid CO_2 and the quick formation of highly porous solid structures within the contact liquid. As illustrated in Fig. 7(f), such porous structures may obstruct the flue gas flow and block the CO_2 desublimation sites. These factors contribute to the insufficient CO_2 desublimation and the slow increase in v_c under low-T_l conditions.

The CO_2 capture performance in a contact liquid is then examined for different flue gas temperatures T_0 ranging from 165 K to 250 K with fixed T_l = 145 K, Y_0 = 1.0, and Pe = 1.4. The simulation results are presented in Fig. 8, including volume fraction of solid CO_2 captured (ϕ_c), outgoing CO_2 content in the gas phase (η_o), the maximum volume fraction of solid CO_2 captured (ϕ_{cm}), the operating time for CO_2 desublimation (t_e), and the CO_2 capture velocity (v_c).

Temporal evolutions of ϕ_c and η_o in Fig. 8(a)–(b) show that both ϕ_c and η_o increase over time for all T_0 values. Additionally, as T_0 drops off, the increase in ϕ_c exhibits only slight changes. It is caused by the restricted availability of CO_2 under the fixed Y_0 and Pe conditions. In contrast, the growth rate of η_o declines significantly with the descending T_0. This can be explained as follows. The cold flue gas shortens the heat transfer period needed for the contact liquid to cool the flue gas from T_0 to the point where CO_2 desublimation begins, ultimately enhancing the CO_2 desublimation process. Combined with the quite stable CO_2 supply, the enhanced CO_2 desublimation process intensifies the CO_2 consumption and thereby yields the declined increase rate of η_o. Such effects of the low-T_0 conditions generally align with those of low-T_l scenarios. By analyzing results of ϕ_c and η_o, the termination states (ϕ_{cm}, t_e) are identified for all tested T_0 values. The obtained ϕ_{cm} and t_e as a function of T_0 are illustrated in Fig. 8(c)–(d), revealing a clear trend that both ϕ_{cm} and t_e decrease as T_0 increases. This is because the cold flue gas intensifies the CO_2 desublimation process and degrades the CO_2 content in the flue gas, which ultimately boosts the generation of solid CO_2 (ϕ_{cm}) and prolongs the duration of CO_2 desublimation (t_e).

The calculated v_c is finally plotted against T_0 in Fig. 8(e), showing that T_0 has a substantial impact on the CO_2 capture efficiency. The decreasing T_0 yields the larger amount of solid CO_2 captured, the longer desublimation period, and the higher CO_2 capture velocity v_c. How-

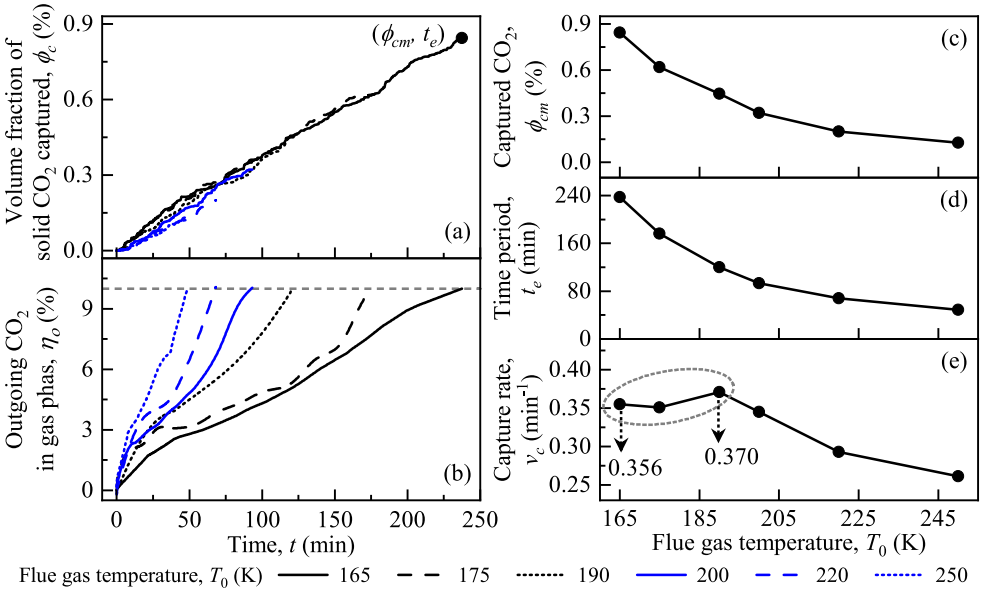

Fig. 8. Analyses of CO_2 capture performance in a contact liquid at T_l = 145 K, $T_0 \in$ [165, 250] K, Y_0 = 1.0, and Pe = 1.4. Temporal evolutions of (a) volume fraction of solid CO_2 captured ϕ_c and (b) outgoing CO_2 content in the gas phase η_o. (c) The maximum volume fraction of solid CO_2 captured ϕ_{cm}. (d) The operation time period for CO_2 desublimation t_e. (e) The CO_2 capture velocity v_c.

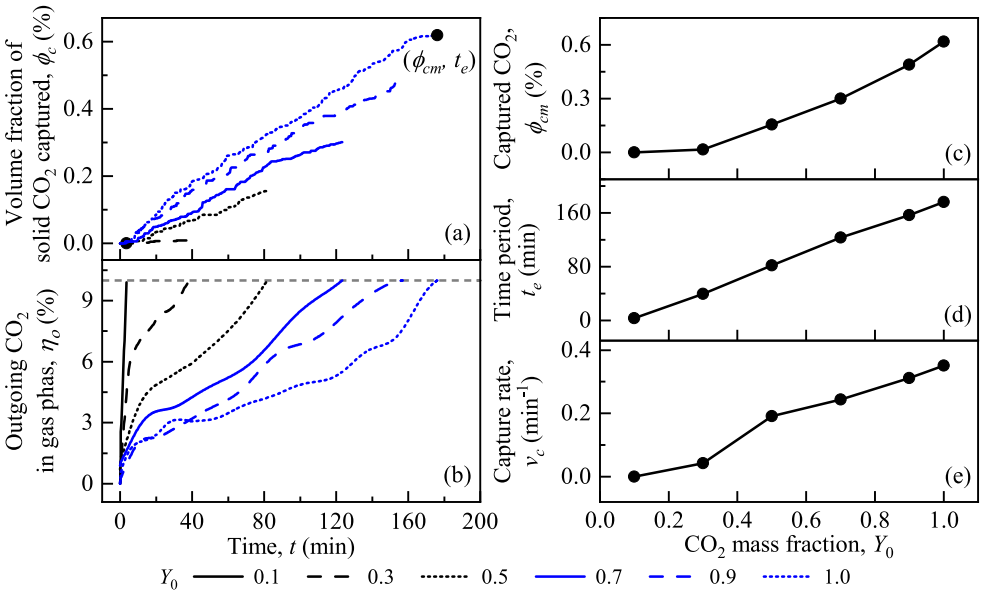

Fig. 9. Analyses of CO_2 capture performance in a contact liquid at T_l = 145 K, T_0 = 175 K, $Y_0 \in$ [0.1, 1.0], and Pe = 1.4. Temporal evolutions of (a) volume fraction of solid CO_2 captured ϕ_c and (b) outgoing CO_2 content in the gas phase η_o. (c) The maximum volume fraction of solid CO_2 captured ϕ_{cm}. (d) The operation time period for CO_2 desublimation t_e. (e) The CO_2 capture velocity v_c.

ever, as T_0 drops from 190 K to 165 K, the positive effect of T_0 becomes marginal, resulting in slight changes in v_c from 0.370 to 0.356. This trend stems from the fact that, although the cold flue gas can intensify the CO_2 desublimation process, the limited CO_2 supply from the injected flue gas restricts the continuous increase in v_c. The discussions in Figs. 7–8 highlight the importance of optimizing temperature levels of both the contact liquid T_l and the flue gas T_0 to enhance the CO_2 capture performance in a contact liquid. It is recommended to avoid excessively low T_l and T_0 values due to the high energy consumption of cooling and their minimal improvements on the CO_2 capture efficiency.

Fig. 9 illustrates the CO_2 capture performance in a contact liquid for varying CO_2 mass fractions Y_0 from 0.1 to 1.0, and fixed T_l = 145 K, T_0 = 175 K, and Pe = 1.4. The temporal evolutions of ϕ_c and η_o for different Y_0 values are illustrated in Fig. 9(a)–(b). The results exhibit a clear trend that the ascending Y_0 boosts the increase in ϕ_c and decelerates the rise in η_o. Consequently, the CO_2 desublimation process completes slowly and the amount of solid CO_2 captured rises rapidly. These substantial effects of Y_0 can be explained as follows. A large Y_0 amplifies the partial pressure $y_i p$ and the Gibbs free energy ΔG, thus speeding up the local CO_2 desublimation rate according to Eq. (12). This consequently contributes to the intensified CO_2 consumption (i.e., the diminished η_o) and the enhanced CO_2 nucleation and growth (i.e., the augmented ϕ_c). Different from the low-T_l or T_o conditions, the high-Y_0 scenarios can increase the CO_2 supply and thus accelerate the growth in ϕ_c obviously. After determining the termination states (ϕ_{cm}, t_e) by using results in Fig. 9(a)–(b), the evolutions of ϕ_{cm}, t_e, and v_c are plotted against Y_0 in Fig. 9(c)–(e). As Y_0 increases, there is a steady growth in all three metrics: ϕ_{cm}, t_e, and v_s. This tend corroborates the above explanation that the high-Y_0 conditions contribute to the improved CO_2 desublimation rate and the enhanced CO_2 capture efficiency.

Attention is finally turned to the influence of gas injection velocity (or Pe) on the CO_2 capture performance. The CO_2 desublimation process in a contact liquid is simulated for varying Pe $\in$ [1.4, 14], and fixed T_l = 145 K, T_0 = 175 K, and Y_0 = 1.0. The modelled results are illustrated in Fig. 10, including evolutions of ϕ_c, η_o, ϕ_{cm}, t_e, and v_c.

Fig. 10 (a)–(b) plot the temporal evolutions of ϕ_c and η_o for different Pe numbers. The data indicates that the consecutive rise in Pe generally causes the rapid increase in ϕ_c. The sufficient supply of CO_2 is responsi-

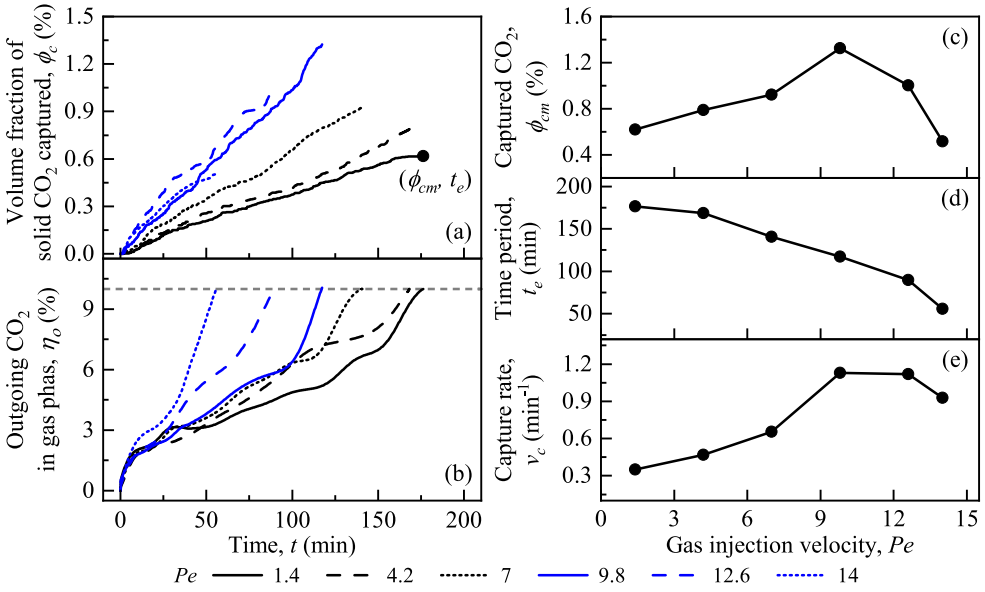

Fig. 10. Analyses of CO_2 capture performance in a contact liquid at T_l = 145 K, T_0 = 175 K, Y_0 = 1.0, and Pe ∈ [1.4, 14]. Temporal evolutions of (a) volume fraction of solid CO_2 captured ϕ_c and (b) outgoing CO_2 content in the gas phase η_o. (c) The maximum volume fraction of solid CO_2 captured ϕ_{cm}. (d) The operation time period for CO_2 desublimation t_e. (e) The CO_2 capture velocity v_c.

ble for this trend. To be specific, the fast gas injection associated with the high-Pe condition intensifies the gas supply and increases the gas phase fraction in the desublimation domain. This subsequently increases the gas–liquid interfaces for CO_2 transport into the liquid, amplifying the number of desublimation sites in the contact liquid. Meanwhile, the local CO_2 desublimation rate remains relatively stable due to the fixed temperature levels and the given CO_2 mass fraction. The combination of these two factors (i.e., the amplified desublimation sites and the stable desublimation rate) boosts the overall CO_2 desublimation rate and accelerates the growth in ϕ_c. However, as Pe continues to ascend beyond an extremely high level (i.e., Pe = 14), the rise in ϕ_c begins to slow down. This occurs because the injected gas flows too fast to allow sufficient time for either the CO_2 transport into the liquid phase for homogeneous desublimation or the heterogeneous CO_2 desublimation on solid surfaces, thereby giving rise to the reduced growth in ϕ_c. On the other hand, a noticeable increase in η_o is detected with the growing Pe. Such an effect is driven by the fact that the barely changed local CO_2 desublimation rate, combined with the significantly increased gas injection velocity, makes much CO_2 remaining in the outgoing flue gas. This subsequently allows the CO_2 desublimation process to complete quickly. The termination states (ϕ_{cm}, t_e, v_c) are plotted against Pe in Fig. 10(c)–(e). A clear trend stands out that both ϕ_{cm} and v_c initially increase with the ascending Pe, but they turn to decline after reaching their peaks at around Pe = 9.8. This pattern stems from the fact that, at an extremely high gas injection velocity (or Pe), the availability of CO_2 in both the liquid phase or the solid surfaces becomes diminished and thereby the CO_2 desublimation efficiency is reduced. Differently, t_e declines progressively as Pe goes up, driven by the rapid rise in η_o under high-Pe conditions.

Based on findings in Figs. 9–10, it is suggested to appropriately select the CO_2 mass fraction Y_0 and the gas injection velocity (or Pe) to optimize the CO_2 capture efficiency of CCC. The CCC system is expected to perform effectively while purifying flue gas with a high CO_2 content (Y_0). This is because a high Y_0 leads to the improved CO_2 desublimation rate and the optimized CO_2 capture efficiency. Meanwhile, a large Pe is favorable since it boosts the overall CO_2 desublimation rate and then improves the CO_2 capture performance. It is emphasized that, however, Pe should not exceed a certain threshold. Beyond this point, the benefits of a high Pe will be degraded due to the limited time for CO_2 transport into the liquid phase or on solid CO_2 surfaces for desublimation. An appropriate Pe is thus essential to balance the enhanced desublimation rate and the degraded CO_2 availability, ensuring the efficient CO_2 capture.

5. Conclusions

In this work, a multiphysics lattice Boltzmann (LB) model has been proposed and validated for pore-scale simulations of CO_2 desublimation in a contact liquid. As a continuation of our recent studies on CO_2 desublimation on solid surfaces (Lei et al., 2023), this work newly introduces the two-phase flow, species transport across the gas and liquid phases, and homogeneous CO_2 desublimation in the contact liquid. Based on the proposed LB model, CO_2 desublimation in a contact liquid is investigated for varying conditions (i.e., the liquid temperature T_l, flue gas temperature T_0, CO_2 mass fraction Y_0, and gas injection velocity (or Pe).

The CO_2 desublimation process is firstly obtained by two-dimensional (2D) simulations. The formation of small solid CO_2 nuclei within the contact liquid and the growth of these nuclei into large solid CO_2 particles are reproduced. Moreover, 3D simulations are carried out to investigate the CO_2 desublimation. The results align well with those from 2D studies, although they come at significantly higher computational costs. It thus confirms the reliability and cost-effectiveness of 2D simulations. After that, a parametric study is carried out to examine effects of operating conditions on the CO_2 capture performance in a contact liquid. With the descending T_l or T_0, there is an obvious growth in the three performance metrics, namely the maximum volume fraction of solid CO_2 captured (ϕ_{cm}), the operation time period (t_e), and the CO_2 capture velocity ($v_c = \phi_{cm}/t_e$). The intensified CO_2 desublimation rate under low-temperature conditions is responsible for this trend. However, when T_l or T_0 drops to extremely low levels, the increase in v_c is constrained by the limited CO_2 supply at the given CO_2 mass fraction Y_0 and gas injection velocity (or Pe). A high Y_0 is found to result in the improved CO_2 desublimation rate and the augmented values of ϕ_{cm}, t_e, and v_c, hence the optimized CO_2 capture efficiency. Following the continuous rise in Pe, t_e decreases consistently, while ϕ_{cm} and v_c increase at first but change to decline after peaking at a threshold. These trends are attributed to the fact that a large Pe can boost the overall CO_2 desublimation rate and improve the CO_2 capture performance. However, such benefits diminish once Pe exceeds the threshold, as the extremely fast gas flow towards the outlet limits the transport of CO_2 to the liquid or solid CO_2 surfaces for desublimation. For the optimal CO_2 capture performance, it is recommended to purify the flue gas with high Y_0 and Pe, while maintaining low T_l and T_0. Nevertheless, extremely low temperatures and excessively high gas injection velocities should be avoided due to the insufficient CO_2 availability in the liquid or on solid surfaces for desublimation.

In summary, the proposed LB model successfully reproduced the CO_2 desublimation processes in a contact liquid during CCC under various operating conditions. The present findings provide valuable insights into the underlying physics of the liquid-based CCC operations and enhance the understanding of optimal conditions. This study demonstrates the capability of LB modelling to facilitate the optimization of CCC, which is a promising technology for mitigating climate change.

Declaration of competing interest

The authors declare that they have no known competing financial interests or personal relationships that could have appeared to influence the work reported in this paper.

CRediT authorship contribution statement

Timan Lei: Data curation, Formal analysis, Investigation, Methodology, Software, Visualization, Validation, Writing – original draft. **Geng Wang:** Investigation, Methodology, Software, Writing – review & editing. **Junyu Yang:** Investigation, Methodology, Software, Writing – review & editing. **Jin Chen:** Writing – review & editing. **Kai H. Luo:** Conceptualization, Formal analysis, Funding acquisition, Investigation, Project administration, Resources, Supervision, Writing – review & editing.

Acknowledgments

This work was supported by the UK Engineering and Physical Sciences Research Council (EPSRC) under the grant No. EP/W026260/1. ARCHER2 supercomputing resources provided by EPSRC under the project "UK Consortium on Mesoscale Engineering Sciences (UKCOMES)" (Grant No. EP/X035875/1) are gratefully acknowledged. This work made use of computational support by CoSeC, the Computational Science Centre for Research Communities, through UKCOMES.

Appendix A. Multiphysics LB model

In this study, the two-dimensional nine-velocity (D2Q9) and three-dimensional nineteen-velocity (D3Q19) MRT LB models are developed for simulating CO_2 desublimation within a contact liquid in two and three dimensions, respectively. The discrete velocities $\boldsymbol{e}_i$, weight coefficients w_i and the transformation matrix $\boldsymbol{M}$ are set as (Guo and Shu, 2013),

$$\text{D2Q9: } \boldsymbol{e}_i = e\begin{bmatrix} 0 & 1 & 0 & -1 & 0 & 1 & -1 & -1 & 1 \\ 0 & 0 & 1 & 0 & -1 & 1 & 1 & -1 & -1 \end{bmatrix}, \tag{A.1}$$

$$\text{D3Q19: } \boldsymbol{e}_i = e\begin{bmatrix} 0 & 1 & -1 & 0 & 0 & 0 & 0 & 1 & -1 & 1 & -1 & 1 & -1 & 1 & -1 & 0 & 0 & 0 & 0 \\ 0 & 0 & 0 & 1 & -1 & 0 & 0 & 1 & 1 & -1 & -1 & 0 & 0 & 0 & 0 & 1 & -1 & 1 & -1 \\ 0 & 0 & 0 & 0 & 0 & 1 & -1 & 0 & 0 & 0 & 0 & 1 & 1 & -1 & -1 & 1 & 1 & -1 & -1 \end{bmatrix}, \tag{A.2}$$

$$\text{D2Q9: } w_i = \begin{cases} 4/9, & i = 0, \\ 1/9, & i = 1-4, \\ 1/36, & i = 5-8, \end{cases} \qquad \text{D3Q19: } w_i = \begin{cases} 1/3, & i = 0, \\ 1/18, & i = 1-6, \\ 1/36, & i = 7-18, \end{cases} \tag{A.3}$$

$$\text{D2Q9: } \boldsymbol{M} = \begin{bmatrix} 1 & 1 & 1 & 1 & 1 & 1 & 1 & 1 & 1 \\ -4 & -1 & -1 & -1 & -1 & 2 & 2 & 2 & 2 \\ 4 & -2 & -2 & -2 & -2 & 1 & 1 & 1 & 1 \\ 0 & 1 & 0 & -1 & 0 & 1 & -1 & -1 & 1 \\ 0 & -2 & 0 & 2 & 0 & 1 & -1 & -1 & 1 \\ 0 & 0 & 1 & 0 & -1 & 1 & 1 & -1 & -1 \\ 0 & 0 & -2 & 0 & 2 & 1 & 1 & -1 & -1 \\ 0 & 1 & -1 & 1 & -1 & 0 & 0 & 0 & 0 \\ 0 & 0 & 0 & 0 & 0 & 1 & -1 & 1 & -1 \end{bmatrix}, \tag{A.4}$$

$$\text{D3Q19: } \boldsymbol{M} = \begin{bmatrix} 1 & 1 & 1 & 1 & 1 & 1 & 1 & 1 & 1 & 1 & 1 & 1 & 1 & 1 & 1 & 1 & 1 & 1 & 1 \\ -30 & -11 & -11 & -11 & -11 & -11 & -11 & 8 & 8 & 8 & 8 & 8 & 8 & 8 & 8 & 8 & 8 & 8 & 8 \\ 12 & -4 & -4 & -4 & -4 & -4 & -4 & 1 & 1 & 1 & 1 & 1 & 1 & 1 & 1 & 1 & 1 & 1 & 1 \\ 0 & 1 & -1 & 0 & 0 & 0 & 0 & 1 & -1 & 1 & -1 & 1 & -1 & 1 & -1 & 0 & 0 & 0 & 0 \\ 0 & -4 & 4 & 0 & 0 & 0 & 0 & 1 & -1 & 1 & -1 & 1 & -1 & 1 & -1 & 0 & 0 & 0 & 0 \\ 0 & 0 & 0 & 1 & -1 & 0 & 0 & 1 & 1 & -1 & -1 & 0 & 0 & 0 & 0 & 1 & -1 & 1 & -1 \\ 0 & 0 & 0 & -4 & 4 & 0 & 0 & 1 & 1 & -1 & -1 & 0 & 0 & 0 & 0 & 1 & -1 & 1 & -1 \\ 0 & 0 & 0 & 0 & 0 & 1 & -1 & 0 & 0 & 0 & 0 & 1 & 1 & -1 & -1 & 1 & 1 & -1 & -1 \\ 0 & 0 & 0 & 0 & 0 & -4 & 4 & 0 & 0 & 0 & 0 & 1 & 1 & -1 & -1 & 1 & 1 & -1 & -1 \\ 0 & 2 & 2 & -1 & -1 & -1 & -1 & 1 & 1 & 1 & 1 & 1 & 1 & 1 & 1 & -2 & -2 & -2 & -2 \\ 0 & -4 & -4 & 2 & 2 & 2 & 2 & 1 & 1 & 1 & 1 & 1 & 1 & 1 & 1 & -2 & -2 & -2 & -2 \\ 0 & 0 & 0 & 1 & 1 & -1 & -1 & 1 & 1 & 1 & 1 & -1 & -1 & -1 & -1 & 0 & 0 & 0 & 0 \\ 0 & 0 & 0 & -2 & -2 & 2 & 2 & 1 & 1 & 1 & 1 & -1 & -1 & -1 & -1 & 0 & 0 & 0 & 0 \\ 0 & 0 & 0 & 0 & 0 & 0 & 0 & 1 & -1 & -1 & 1 & 0 & 0 & 0 & 0 & 0 & 0 & 0 & 0 \\ 0 & 0 & 0 & 0 & 0 & 0 & 0 & 0 & 0 & 0 & 0 & 0 & 0 & 0 & 0 & 1 & -1 & -1 & 1 \\ 0 & 0 & 0 & 0 & 0 & 0 & 0 & 0 & 0 & 0 & 0 & 1 & 1 & -1 & -1 & 0 & 0 & 0 & 0 \\ 0 & 0 & 0 & 0 & 0 & 0 & 0 & 1 & -1 & 1 & -1 & -1 & 1 & -1 & 1 & 0 & 0 & 0 & 0 \\ 0 & 0 & 0 & 0 & 0 & 0 & 0 & -1 & -1 & 1 & 1 & 0 & 0 & 0 & 0 & 1 & -1 & 1 & -1 \\ 0 & 0 & 0 & 0 & 0 & 0 & 0 & 0 & 0 & 0 & 0 & 1 & 1 & -1 & -1 & -1 & -1 & 1 & 1 \end{bmatrix}. \tag{A.5}$$

Here $e = \delta_x/\delta_t$ is the lattice speed and it is set as $e = 1$ in this study. δ_x and δ_t denote the lattice spacing and time step, respectively.

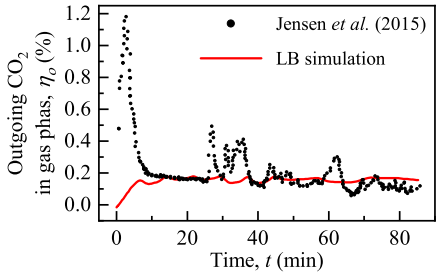

Fig. 11. Model validation of CO_2 desublimation in a contact liquid. Comparison of the outgoing CO_2 content in the gas phase η_o between the present numerical results and the experimental measurements by Jensen et al. (2015).

The transformation matrix $\boldsymbol{M}$ maps distribution functions from the physical space $\boldsymbol{\psi}$ to the moment space as $\hat{\boldsymbol{\psi}} = \boldsymbol{M} \cdot \boldsymbol{\psi}$. With this transformation, the evolution Eqs. (20)–(23) are performed in the moment space as,

$$\hat{\boldsymbol{f}}\left(\boldsymbol{x}+\boldsymbol{e}_i\delta_t,\ t+\delta_t\right) = \hat{\boldsymbol{f}}(\boldsymbol{x},\ t) - \boldsymbol{S}\left[\hat{\boldsymbol{f}}(\boldsymbol{x},\ t) - \hat{\boldsymbol{f}}^{eq}(\boldsymbol{x},\ t)\right] + \delta_t \hat{\boldsymbol{F}}, \tag{A.6}$$

$$\hat{\boldsymbol{p}}\left(\boldsymbol{x}+\boldsymbol{e}_i\delta_t,\ t+\delta_t\right) = \hat{\boldsymbol{p}}(\boldsymbol{x},\ t) - \boldsymbol{S}_\phi\left[\hat{\boldsymbol{p}}(\boldsymbol{x},\ t) - \hat{\boldsymbol{p}}^{eq}(\boldsymbol{x},\ t)\right] + \delta_t \hat{\boldsymbol{F}}_p, \tag{A.7}$$

$$\hat{\boldsymbol{g}}\left(\boldsymbol{x}+\boldsymbol{e}_i\delta_t,\ t+\delta_t\right) = \hat{\boldsymbol{g}}(\boldsymbol{x},\ t) - \boldsymbol{S}_y\left[\hat{\boldsymbol{g}}(\boldsymbol{x},\ t) - \hat{\boldsymbol{g}}^{eq}(\boldsymbol{x},\ t)\right] + \delta_t \hat{\boldsymbol{F}}_y, \tag{A.8}$$

$$\hat{\boldsymbol{h}}\left(\boldsymbol{x}+\boldsymbol{e}_i\delta_t,\ t+\delta_t\right) = \hat{\boldsymbol{h}}(\boldsymbol{x},\ t) - \boldsymbol{S}_t\left[\hat{\boldsymbol{h}}(\boldsymbol{x},\ t) - \hat{\boldsymbol{h}}^{eq}(\boldsymbol{x},\ t)\right] + \delta_t \hat{\boldsymbol{F}}_t. \tag{A.9}$$

Through the Chapman-Enskog analysis on the proposed LB equations, the governing equations can be recovered with the relaxation times τ, τ_ϕ, τ_y, and τ_t being,

$$\nu = c_s^2(\tau-0.5)\delta_t,\ M = c_s^2\left(\tau_\phi-0.5\right)\delta_t,\ D = c_s^2\left(\tau_y-0.5\right)\delta_t,\ \alpha = c_s^2\left(\tau_t-0.5\right)\delta_t, \tag{A.10}$$

as well as the gradient terms of temperature being (Lei et al., 2017; 2021),

$$\nabla_x T = -\frac{\hat{h}_3 - Tu}{c_s^2\tau_t\delta_t}, \qquad \nabla_y T = -\frac{\hat{h}_5 - Tv}{c_s^2\tau_t\delta_t}. \tag{A.11}$$

Except these calculations, other gradient terms and Laplace operates in Section 3 are calculated by the isotropic central scheme as (Guo et al., 2011),

$$\nabla\varsigma = \sum_i \frac{w_i\boldsymbol{e}_i\varsigma\left(\boldsymbol{x}+\boldsymbol{e}_i\delta_t\right)}{c_s^2\delta_t}, \qquad \nabla^2\varsigma = \sum_i \frac{2w_i\varsigma\left(\boldsymbol{x}+\boldsymbol{e}_i\delta_t\right) - \varsigma(\boldsymbol{x})}{c_s^2\delta_t^2}. \tag{A.12}$$

Appendix B. Model validation

We have recently developed LB models for simulating CO_2 desublimation in a packed bed during CCC (Lei et al., 2023; 2024). Benchmark problems with analytical or experimental solutions have been conducted to test key sub-models of this proposed LB models. For brevity, these validation details are not repeated here. Building on our prior studies, this research extends the LB models to include two-phase flow, species transport across phases, and homogeneous desublimation, thereby allowing simulations of CO_2 desublimation in a contact liquid. To validate the reliability of the newly proposed LB model, we simulated the CO_2 desublimation process based on the desublimation domain in Fig. 1.

Our simulations are conducted as described in Section 3 of Jensen et al. (2015), with the same desublimation conditions applied. Specifically, the flue gas temperature $T_0 = 145$ K, CO_2 mass fraction $Y_0 = 0.15$, and the gas pressure $p_0 = 1$ atm. The thermophysical properties are set as in Section 4. The outgoing CO_2 content in the flue gas (η_o) is calculated and plotted against time in Fig. 11, where the experimental data from Jensen et al. (2015) is included for comparison. As shown, the experimental data exhibits several peaks that are not present in our simulations. According to Jensen et al. (2015), these peaks are resulted from changes in operating conditions during experiments. Despite these discrepancies, the proposed LB model successfully replicates the overall CO_2 capture performance observed in experiments, demonstrating its accuracy in simulating CO_2 desublimation in a contact liquid.

References

Ali, A., Maqsood, K., Redza, A., Hii, K., Shariff, A.B.M., Ganguly, S., 2016. Performance enhancement using multiple cryogenic desublimation based pipeline network during dehydration and carbon capture from natural gas. Chem. Eng. Res. Des. 109, 519–531. doi:10.1016/j.cherd.2016.01.020.

Ali, A., Maqsood, K., Syahera, N., Shariff, A.B.M., Ganguly, S., 2014. Energy minimization in cryogenic packed beds during purification of natural gas with high CO_2 content. Chem. Eng. Technol. 37 (10), 1675–1685. doi:10.1002/ceat.201400215.

Bose, D., Bhattacharya, R., Kaur, T., Pandya, R., Sarkar, A., Ray, A., Mondal, S., Mondal, A., Ghosh, P., Chemudupati, R.I., 2024. Innovative approaches for carbon capture and storage as crucial measures for emission reduction within industrial sectors. Carbon Capture Sci. Technol. 12, 100238. doi:10.1016/j.ccst.2024.100238.

Chen, L., He, A., Zhao, J.L., Kang, Q.J., Li, Z.Y., Carmeliet, J., Shikazono, N., Tao, W.Q., 2022. Pore-scale modeling of complex transport phenomena in porous media. Prog. Energy Combust. Sci. 88, 100968. doi:10.1016/j.pecs.2021.100968.

Chen, L., Kang, Q.J., Carey, B., Tao, W.Q., 2014. Pore-scale study of diffusion-reaction processes involving dissolution and precipitation using the lattice Boltzmann method. Int. J. Heat Mass Transf. 75, 483–496. doi:10.1016/j.ijheatmasstransfer.2014.03.074.

Chen, L., Zhang, R.Y., Kang, Q.J., Tao, W.Q., 2020. Pore-scale study of pore-ionomer interfacial reactive transport processes in proton exchange membrane fuel cell catalyst layer. Chem. Eng. J. 391, 123590. doi:10.1016/j.cej.2019.123590.

Debnath, B., Mukherjee, A., Mullick, A., Ghoshdastidar, S., Ganguly, S., Kargupta, K., 2019. Desublimation based separation of CO_2 inside a cryogenic packed bed: performance mapping with the spatiotemporal evolution of CO_2 frost. Chem. Eng. Res. Des. 146, 166–181. doi:10.1016/j.cherd.2019.03.024.

Fazlollahi, F., Saeidi, S., Safdari, M.-S., Sarkari, M., Klemeš, J.J., Baxter, L.L., 2017. Effect of operating conditions on cryogenic carbon dioxide removal. Energy Technol. 5 (9), 1588–1598. doi:10.1002/ente.201600802.

Font-Palma, C., Cann, D., Udemu, C., 2021. Review of cryogenic carbon capture innovations and their potential applications. J. Carbon Res. 7 (3), 58. doi:10.3390/c7030058.

Guo, Z.L., Shu, C., 2013. Lattice Boltzmann Method and its Applications in Engineering. World Scientific Publisher, Singapore, Singapore.

Guo, Z.L., Zheng, C.G., Shi, B.C., 2011. Force imbalance in lattice Boltzmann equation for two-phase flows. Phys. Rev. E 83 (3), 036707. doi:10.1103/PhysRevE.83.036707.

He, Y.L., Liu, Q., Li, Q., Tao, W.Q., 2019. Lattice Boltzmann methods for single-phase and solid-liquid phase-change heat transfer in porous media: a review. Int. J. Heat Mass Transf. 129, 160–197. doi:10.1016/j.ijheatmasstransfer.2018.08.135.

Jensen, M.J., 2015. Energy Processes Enabled by Cryogenic Carbon Capture. Brigham Young University.

Jensen, M.J., Russell, C.S., Bergeson, D., Hoeger, C.D., Frankman, D.J., Bence, C.S., Baxter, L.L., 2015. Prediction and validation of external cooling loop cryogenic carbon capture (CCC-ECL) for full-scale coal-fired power plant retrofit. Int. J. Greenhouse Gas Control 42, 200–212. doi:10.1016/j.ijggc.2015.04.009.

Kamkeng, A.D.N., Wang, M.H., Hu, J., Du, W.L., Qian, F., 2021. Transformation technologies for CO_2 utilisation: current status, challenges and future prospects. Chem. Eng. J. 409, 128138. doi:10.1016/j.cej.2020.128138.

Kang, Q.J., Chen, L., Valocchi, A.J., Viswanathan, H.S., 2014. Pore-scale study of dissolution-induced changes in permeability and porosity of porous media. J. Hydrol. (Amst) 517, 1049–1055. doi:10.1016/j.jhydrol.2014.06.045.

Kang, Q.J., Lichtner, P.C., Zhang, D.X., 2006. Lattice Boltzmann pore-scale model for multicomponent reactive transport in porous media. J. Geophys. Res. Solid Earth 111 (B5), B05203. doi:10.1029/2005JB003951.

Karani, H., Huber, C., 2015. Lattice Boltzmann formulation for conjugate heat transfer in heterogeneous media. Phys. Rev. E 91 (2), 023304. doi:10.1103/PhysRevE.91.023304.

Lei, T., Luo, K.H., Hernández Pérez, F.E., Wang, G., Wang, Z., Restrepo Cano, J., Im, H.G., 2023. Study of CO_2 desublimation during cryogenic carbon capture using the lattice Boltzmann method. J. Fluid Mech. 964, A1. doi:10.1017/jfm.2023.227.

Lei, T., Luo, K.H., Pérez, F.E.H., Wang, G., Yang, J., Cano, J.R., Im, H.G., 2024. Pore-scale study of CO_2 desublimation and sublimation in a packed bed during cryogenic carbon capture. J. Fluid Mech. 990, A6. doi:10.1017/jfm.2024.351.

Lei, T., Luo, K.H., Wu, D., 2019. Generalized lattice Boltzmann model for frosting. Phys. Rev. E 99 (5), 053301. doi:10.1103/PhysRevE.99.053301.

Lei, T., Meng, X.H., Guo, Z.L., 2017. Pore-scale study on reactive mixing of miscible solutions with viscous fingering in porous media. Comput. Fluids 155, 146–160. doi:10.1016/j.compfluid.2016.09.015.

Lei, T., Wang, Z., Luo, K.H., 2021. Study of pore-scale coke combustion in porous media using lattice Boltzmann method. Combust. Flame 225, 104–119. doi:10.1016/j.combustflame.2020.10.036.

Li, Q., Luo, K.H., Kang, Q.J., He, Y.L., Chen, Q., Liu, Q., 2016. Lattice Boltzmann methods for multiphase flow and phase-change heat transfer. Prog. Energy Combust. Sci. 52, 62–105. doi:10.1016/j.pecs.2015.10.001.

Liang, H., Xu, J., Chen, J., Wang, H., Chai, Z., Shi, B., 2018. Phase-field-based lattice Boltzmann modeling of large-density-ratio two-phase flows. Phys. Rev. E 97 (3), 033309. doi:10.1103/PhysRevE.97.033309.

Mac Dowell, N., Fennell, P.S., Shah, N., Maitland, G.C., 2017. The role of CO_2 capture and utilization in mitigating climate change. Nat. Clim. Chang 7 (4), 243–249. doi:10.1038/NCLIMATE3231.

Naquash, A., Qyyum, M.A., Haider, J., Bokhari, A., Lim, H., Lee, M., 2022. State-of-the-art assessment of cryogenic technologies for biogas upgrading: energy, economic, and environmental perspectives. Renew. Sustain. Energy Rev. 154, 111826. doi:10.1016/j.rser.2021.111826.

Pan, X.Q., Clodic, D., Toubassy, J., 2013. CO_2 Capture by antisublimation process and its technical economic analysis. Greenhouse Gases Sci. Technol. 3 (1), 8–20. doi:10.1002/ghg.1313.

Song, C.F., Kitamura, Y., Li, S.H., 2012a. Evaluation of Stirling cooler system for cryogenic CO_2 capture. Appl Energy 98, 49–501. doi:10.1016/j.apenergy.2012.04.013.

Song, C.F., Kitamura, Y., Li, S.H., 2014. Optimization of a novel cryogenic CO_2 capture process by response surface methodology (RSM). J. Taiwan Inst. Chem. Eng. 45 (4), 1666–1676. doi:10.1016/j.jtice.2013.12.009.

Song, C.F., Kitamura, Y., Li, S.H., Jiang, W.Z., 2013. Analysis of CO_2 frost formation properties in cryogenic capture process. Int. J. Greenhouse Gas Control 13, 26–33. doi:10.1016/j.ijggc.2012.12.011.

Song, C.F., Kitamura, Y., Li, S.H., Ogasawara, K., 2012b. Design of a cryogenic CO_2 capture system based on Stirling coolers. Int. J. Greenhouse Gas Control 7, 107–114. doi:10.1016/j.ijggc.2012.01.004.

Tuinier, M.J., Hamers, H.P., van Sint Annaland, M., 2011a. Techno-economic evaluation of cryogenic CO_2 capture-A comparison with absorption and membrane technology. Int. J. Greenhouse Gas Control 5 (6), 1559–1565. doi:10.1016/j.ijggc.2011.08.013.

Tuinier, M.J., van Sint Annaland, M., Kramer, G.J., Kuipers, J.A.M., 2010. Cryogenic CO_2 capture using dynamically operated packed beds. Chem. Eng. Sci. 65 (1), 114–119. doi:10.1016/j.ces.2009.01.055.

Tuinier, M.J., van Sint Annaland, M., Kuipers, J.A.M., 2011b. A novel process for cryogenic CO_2 capture using dynamically operated packed beds-An experimental and numerical study. Int. J. Greenhouse Gas Control 5 (4), 694–701. doi:10.1016/j.ijggc.2010.11.011.

Wang, G., Fei, L., Lei, T., Wang, Q., Luo, K.H., 2022. Droplet impact on a heated porous plate above the Leidenfrost temperature: a lattice Boltzmann study. Physics of Fluids 34 (9). doi:10.1016/j.ijmultiphaseflow.2023.10458.

Wang, G., Yang, J., Lei, T., Chen, J., Wang, Q., Luo, K.H., 2023. A three-dimensional non-orthogonal multiple-relaxation-time phase-field lattice Boltzmann model for multiphase flows at large density ratios and high Reynolds numbers. Int. J. Multiphase Flow 168, 104582. doi:10.1063/5.0118079.

Wang, J.K., Wang, M.R., Li, Z.X., 2007. A lattice Boltzmann algorithm for fluid-solid conjugate heat transfer. Int. J. Therm. Sci. 46 (3), 228–234. doi:10.1016/j.ijthermalsci.2006.04.012.

Wang, M.R., Pan, N., 2008. Modeling and prediction of the effective thermal conductivity of random open-cell porous foams. Int. J. Heat Mass Transf. 51 (5–6), 1325–1331. doi:10.1016/j.ijheatmasstransfer.2007.11.031.

Wang, Q.L., Han, D.Y., Wang, Z.M., Ma, Q.S., Wang, D.Y., 2019. Lattice Boltzmann modeling for hydrate formation in brine. Chem. Eng. J. 366, 133–140. doi:10.1016/j.cej.2019.02.060.

Wei, X.Q., Li, W.Z., Liu, Q.Y., Sun, W.T., Liu, S.W., Li, S., Wei, H.Y., Ma, L.L., 2022. Pore-scale investigation on multiphase reactive transport for the conversion of levulinic acid to γ-valerolactone with Ru/C catalyst. Chem. Eng. J. 427, 130917. doi:10.1016/j.cej.2021.130917.

Xu, Q.H., Long, W., Jiang, H., Ma, B., Zan, C., Ma, D.S., Shi, L., 2018a. Quantification of the microstructure, effective hydraulic radius and effective transport properties changed by the coke deposition during the crude oil in-situ combustion. Chem. Eng. J. 331, 856–869. doi:10.1016/j.cej.2017.09.002.

Xu, Q.H., Long, W., Jiang, H., Zan, C., Huang, J., Chen, X., Shi, L., 2018b. Pore-scale modelling of the coupled thermal and reactive flow at the combustion front during crude oil in-situ combustion. Chem. Eng. J. 350, 776–790. doi:10.1016/j.cej.2018.04.114.

Yang, J., Lei, T., Wang, G., Xu, Q., Chen, J., Luo, K.H., 2023. Lattice boltzmann modelling of salt precipitation during brine evaporation. Adv. Water Resour. 180, 104542. doi:10.1016/j.advwatres.2023.104542.

Yang, J.-Y., Dai, X.-Y., Xu, Q.-H., Liu, Z.-Y., Shi, L., 2022. Comparative investigation of a lattice Boltzmann boundary treatment of multiphase mass transport with heterogeneous chemical reactions. Phys. Rev. E 105 (5), 055302. doi:10.1103/PhysRevE.105.055302.

Yang, J.Y., Dai, X.Y., Xu, Q.H., Liu, Z.Y., Zan, C., Long, W., Shi, L., 2021. Pore-scale study of multicomponent multiphase heat and mass transfer mechanism during methane hydrate dissociation process. Chem. Eng. J. 423, 130206. doi:10.1016/j.cej.2021.130206.

Zhang, L.M., Zhang, C.D., Zhang, K., Zhang, L., Yao, J., Sun, H., Yang, Y.F., 2019. Pore-Scale investigation of methane hydrate dissociation using the lattice Boltzmann method. Water Resour. Res. 55 (11), 8422–8444. doi:10.1029/2019WR025195.

Zhang, T., Shi, B.C., Guo, Z.L., Chai, Z.H., Lu, J.H., 2012. General bounce-back scheme for concentration boundary condition in the lattice-Boltzmann method. Phys. Rev. E 85 (1), 016701. doi:10.1103/PhysRevE.85.016701.